3D Printing of Multi-Material Structures: FY17 Line-Supported Novel & Engineered Materials Program

E.M. Parsons
T.M. Mower
J.W. Schoenenberger
J.C. Weinberg
J.A. Wellman
A.J. Hart
J. Beroz
J. Rothman

17 January 2018

Lincoln Laboratory

MASSACHUSETTS INSTITUTE OF TECHNOLOGY

LEXINGTON, MASSACHUSETTS

Massachusetts Institute of Technology
Lincoln Laboratory

3D Printing of Multi-Material Structures: FY17 Line-Supported Novel & Engineered Materials Program

E.M. Parsons
T.M. Mower
J.W. Schoenenberger
J.C. Weinberg
J.A. Wellman
Group 74

A.J. Hart
J. Beroz
J. Rothman
MIT Department of Mechanical Engineering

Project Report LSP-213

17 January 2018

Lexington   Massachusetts

This page intentionally left blank.

TABLE OF CONTENTS

Page

TABLE OF CONTENTS
(Continued)

LIST OF FIGURES

LIST OF FIGURES

(Continued)

LIST OF FIGURES
(Continued)

LIST OF FIGURES

(Continued)

viii

**Figure
No.**

Page

This page intentionally left blank.

1. 3D PRINTING OF MULTI-MATERIAL STRUCTURES: INTRODUCTION

The need to miniaturize unmanned areal vehicles, satellites, and devices requires shaping metals or ceramics into complex, three-dimensional geometries for applications such as electrically small antennae, inductors, microactuators, micro heat exchangers, thermal shielding elements, and integrated thermomechanical packaging. However, the optimum shape of these components or structures is frequently not practical or even possible with conventional manufacturing methods. Internal features and three-dimensional cellular geometries cannot be manufactured by machining or lithography. Furthermore, performance of a component or structure can often be further improved by constructing it from two or more dissimilar materials. For example, a temperature resistant ceramic can be coated or bonded onto a low density metal to optimize both thermal and structural performance. Difficulties also arise in this case because bonding materials or coating internal surfaces is challenging and the interface between two materials is typically a point of stress concentration and weakness. Far preferable would it be to have the capability to transition smoothly from one material to another, avoiding stepped interfaces, to create what is known as a functionally graded material. (A sharp transition in certain properties, such as magnetism, can actually be desirable.) Three-dimensional (3D) printing has the potential to manufacture these complex parts with controlled composition and functionality, but the resolution, surface finish, and multi-material capability of current 3D printing technologies are insufficient. This project therefore sought to develop a high resolution method of 3D printing metals, ceramics, and metal-ceramic composites.

3D printing has had substantial impact on numerous sectors at scales ranging from microfabrication to big area manufacturing (size of meters). Many predict that it will soon be recognized as the technology behind the third industrial revolution. It is defined by the ISO/ASTM as "the process of joining materials to make parts from 3D model data, usually layer upon layer, as opposed to subtractive and formative manufacturing methodologies." With 3D printing, parts of complex geometry can be built with a single machine operation and without any special masks, tooling, dies, or fixtures. Originally used primarily for fabrication of prototyps and models of design concepts, various 3D printing methods are presently capable of producing functional devices, components, and structures constructed from a range of material types. In fact, data published in the 2017 Wohlers Report show that the most common use of 3D printing is the fabrication of functional parts (33.8% of applications, and 60.6% of the market for an estimated $3.6 billion [10]).

The first and most advanced application of 3D printing technology is the production of polymer parts. Via extrusion, photopolymerization, or fusion, parts can be fabricated from a variety of different polymers, including thermoplastics, thermosets, and polymer matrix composites. Methods that use material jetting followed by a photocure step can rapidly print multiple materials in one build. With vat polymerization, printing multiple materials is time consuming, but the build

resolution can be as good or better than it is with conventional fabrication methods ($<1-2\,\mu$m with microstereolithography and about $50\,$nm with two-photon polymerization).

3D printing of metals and ceramics has been much slower to develop than printing of polymers has been, but production of final parts by printing of metals is now increasing rapidly. The most common and highest resolution form of metal printing is selective laser melting (SLM), a powder bed fusion process in which selective areas of a powder bed are melted and fused with a high energy laser (Figure 1). Once fusion of a given layer is complete, the build platform is lowered, and another layer is spread or "recoated" over the platform. A similar process, selective laser sintering (SLS), can be used to fuse ceramics by sintering—not full melting. SLM has recently been adopted by the Laboratory and is ideal for the production of low volumes of high value parts, typical of the defense and aerospace sectors. Heavily light-weighted parts and parts with internal channels or cavities can be manufactured, sometimes reducing to a single piece an assembly that would otherwise consist of dozens of separate components joined together. In many cases, SLM enables fabrication of parts with complex features that could not be produced at all with conventional methods.
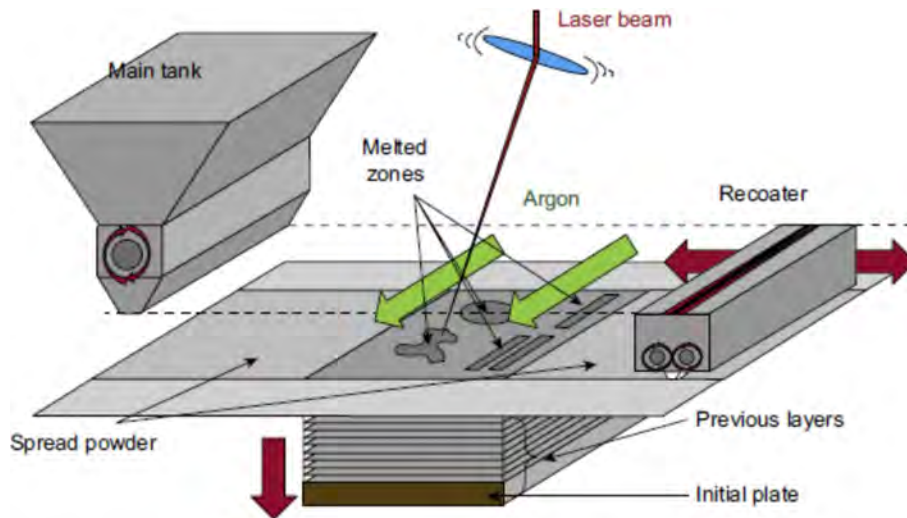
Figure 1. Schematic of the build chamber of a selective laser melting machine, showing the laser beam, build plate, powder recoater, and flow of inert gas [9]. This example uses a hopper to deposit powder (top left), similar to the design of the micro-SLM.

In spite of the many advantages of these powder bed fusion processes, the relatively low resolution, poor surface finish, and single material capability of commercial SLM systems prevent their use in many critical applications. The minimum feature size or resolution, typically $250-500\,\mu$m, is limited by the spot size of the laser beam, $d_{\mathrm{beam}} \geq 80\,\mu$m in most cases, and the diameter of

the powder particles, typically $15-45\,\mu$m. The average surface roughness in the build plane is $R_\mathrm{a} = 10-20\,\mu$m, and the roughness is much higher at the other surfaces due to the "stair-step" (ribbed) effect caused by interlayer misalignment. Moreover, the number of materials commercially available for SLM is small, fewer than 20 still, and no SLM machine can process more than one material during a build. Because the technology to manufacture complex, multi-material components and structures at high resolution did not exist, the goal of this project was to develop the processes and materials required to 3D print these parts with laser powder bed fusion.

The proposed process, termed micro selective laser melting (micro-SLM), would be similar to commercial SLM processes, but it was envisioned to have: (1) a greater than 10 times improvement in spatial resolution, enabling the printing of features measuring as small as $10\,\mu$m; (2) the capability to deposit microparticles of a second material (metal or ceramic) into the powder bed at similar spatial resolution (Figure 2). The conceptualized improvement in resolution was attributed to the use of a laser spot size of only $10\,\mu$m and a powder bed composed of particles with an average diameter of less than $10\,\mu$m. The deposition of the second phase material was designed to occur by electrohydrodynamic printing of individual microparticles with diameter of about $1-10\ \mu$m. As such, the powder bed could be selectively modified by the microparticles in areas where the fused part required a change of material properties. Alternatively, the volume fractions of powder and microparticles delivered to the build platform for each layer could be continuously varied so that the fused material composition would transition smoothly from the composition of the powder bed to the composition of the microparticles. It was foreseen that the ability to control finely the distribution of material in the powder bed would enable the fabrication of new alloys, metal-ceramic composites, and functionally graded materials.

The remainder of this document is organized as follows: Section 2 describes the completion and characterization of the micro-SLM system with capability to fuse single layer samples. A unique feature of this machine is that fusion can be conducted with a continuous wave laser beam and a pulsed laser beam that are coaligned. Section 3 discusses the importance for powder bed fusion of starting with a dense, homogeneous powder bed and describes work undertaken to determine the optimum particle properties and powder bed recoating methods. Section 4 presents the results of single track melting trials that demonstrate that the micro-SLM can laser weld stainless steel plate and fuse single layers of stainless steel powder. Section 5 presents an analytical model of the laser heating process and uses the derived scaling relations to predict the micro-SLM process parameters. Section 6 describes the work undertaken at MIT to develop a high-rate method to deposit individual microparticles onto a substrate with micron-level precision. Section 7, the conclusion of the document, highlights this year's successes and describes plans for future research on 3D printing of high performance structural materials.
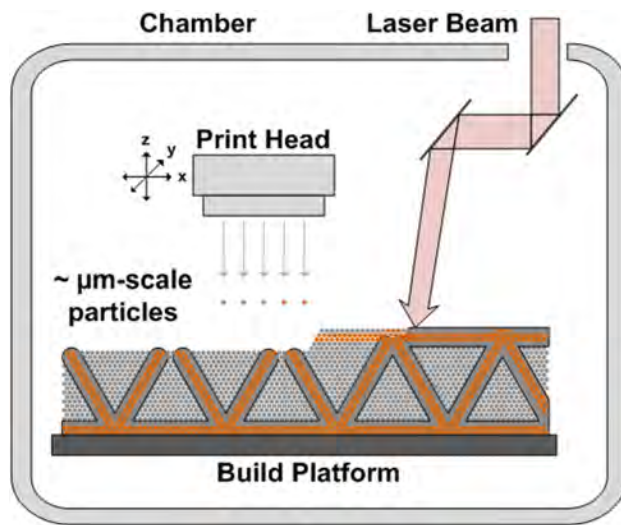
Figure 2. Schematic of envisioned multi-material 3D printing method, with printhead depositing particles onto the build plane just before laser fusion occurs.

2. ASSEMBLY AND CHARACTERIZATION OF THE MICRO SELECTIVE LASER MELTING SYSTEM (MICRO-SLM)

This section documents progress toward designing and building a custom, open architecture system for consolidating multi-material powders at high resolution with powder bed fusion. Fusion of metals, ceramics, and combinations thereof was envisioned by either full melting (metal phase) or sintering (ceramic phase). The system would function similarly to existing commercial selective laser melting machines, but the architecture was designed to enable fusion of powders consisting of different powder materials within a single layer. The multi-material capability would be provided by a novel electrohydrodynamic printing method, termed digital particle ejection (John Hart, MIT), that can directly deposit single particles of diameter $1-10$ μm with high throughput ($\sim$10 kHz) and high positioning resolution. With this method, after spreading of a layer of powder, particles of a second material could be precisely placed into the powder bed before the powder bed was selectively fused in order to optimize the properties of the material or structure (Figure 3).
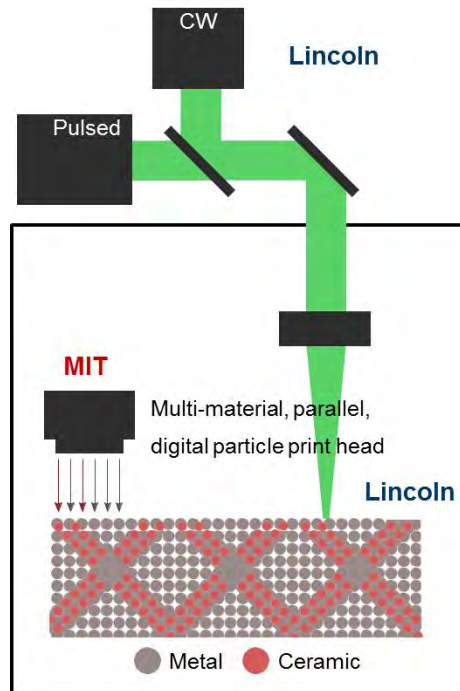
Figure 3. Schematic of micro-SLM system showing combined continuous wave (CW) laser and pulsed laser for control of both melting and powder bed compaction.

5

In addition to multi-material capability, a second ambitious goal for the system was an unprecedented high print resolution for an SLM process. Through the use of fine particles (diameter less than $\sim 10\,\mu$m) and a laser spot size of only about $10\,\mu$m, a positioning resolution and feature size on the order of $10\,\mu$m were sought. The system was therefore dubbed the "micro-SLM." A significant challenge in the fusion of fine powders is the preparation of a sufficiently dense and uniform layer of powder each time the build platform is recoated with powder. As the size of the particles decreases, interparticle cohesive forces and friction become dominant over gravitational forces, causing the powder to clump together and pack poorly. Recent results in the literature show direct correlations between the uniformity and relative density of the powder bed and the relative density of the fused material, which should be a minimum of 99% in SLM. In an effort to achieve high relative density with fine powders, the system was designed to use both a continuous wave (CW) laser and a pulsed laser simultaneously. The CW laser would heat or melt the metal powders, and the pulsed laser would supply additional energy for melting and vaporization of the metal. It was hoped that the large pressure exerted on the melt pool by the expanding metal vapor (known as recoil pressure) would compact the powder bed as fusion occurred, resulting in a solidified material with low porosity.
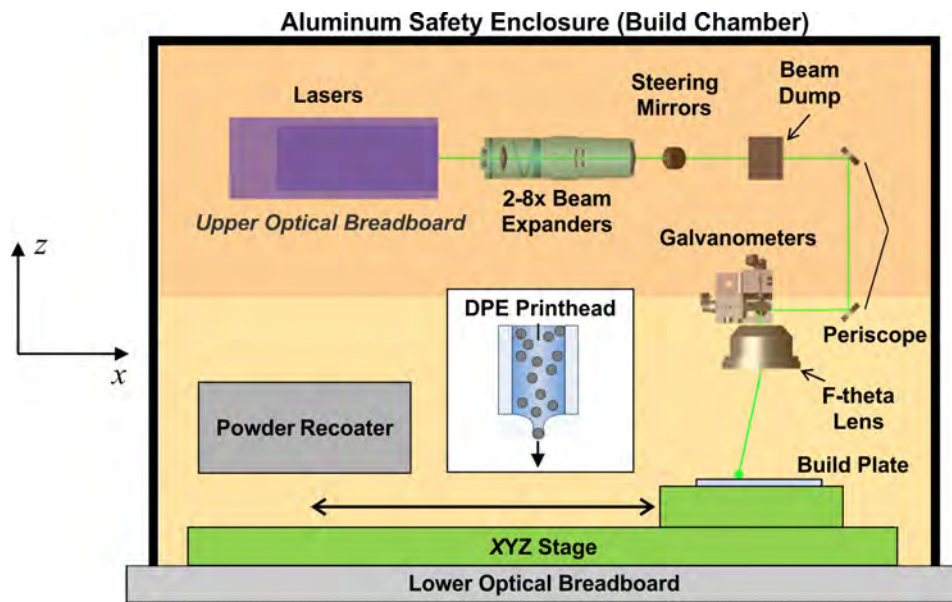
Figure 4. Schematic of envisioned micro-SLM system, including laser energy sources, beam steering system, build platform, build chamber, powder delivery system, and printhead for deposition of single microparticles.

2.1 DESIGN AND ASSEMBLY OF THE MICRO-SLM SYSTEM HARDWARE

Design and assembly of the basic hardware for the single material micro-SLM system were completed in FY 2017. The system is currently capable of fusing or sintering single layer samples. The printhead for digital particle ejection (DPE printhead) is still under development at MIT but could be added at a later date.

The micro-SLM system hardware, like that of any powder bed fusion machine, consists of five major components: a laser energy source, a beam steering system, a build platform, a build chamber, and a powder delivery system (Table 1). The layout of the system components was designed such that the DPE printhead could eventually be integrated with the micro-SLM machine. As shown schematically in Figure 5, all the components are contained within an enclosure constructed from aluminum bars and panels that serves as a build chamber. The lasers and a portion of the optical components are fixed to an optical breadboard that is raised on optical posts above a second, larger optical breadboard. The beam steering system guides the laser beam from the laser down to the build area, the $70\,\text{mm} \times 70\,\text{mm}$ area over which the laser can scan in focus. The build plate, where the powder is first spread (or printed eventually), is fixed to a 3-axis linear translation stage. Together, the build plate and the translation stage make up the build platform, which is fixed to the optical breadboard. After each layer of powder is selectively fused, the translation stage lowers the build plate and translates the stage horizontally (x-direction) over to the powder recoater, where the next layer of powder is deposited and spread. The DPE printhead would simply be another stop for the translation stage to make. In the following sections, each of the first four major components is described in further detail. Discussion of the powder delivery system is delayed until Section 3.

TABLE 1

Major Components and Key Specifications of the Micro-SLM System

Component	Manufacturer	Model	Specifications
Continuous wave laser	Opto Engine	MGL-N-532A	P=5 W, λ=532 nm
Pulsed laser	Bright Solutions	WEDGE HF	P=1-2 W, t_{pulse}=0.5-2 ns, f=40-200 kHz, λ=532 nm
F-theta lens	Eskimo Optics	150-1002	L_{focus}=100 mm, w.d.=115 mm
Dual-axis galvanometer	Cambridge Tech.	6220HM40B	40° optical scan angle
Build platform stages	Zaber	T-LSM100A	0.048 μm res., 101.6 mm travel
Build chamber	80/20 Inc.	#1010	0.125" aluminum panels
Powder delivery	Newport, ASI	custom	fully adjustable

2.1.1 Lasers and beam steering system

A continuous wave laser and pulsed laser are combined to supply the energy to fuse the powder on the build plate (Figure 5). The CW laser is an $532\,\mathrm{nm}$, $5\,\mathrm{W}$ all-solid-state laser. The pulsed laser is a $532\,\mathrm{nm}$ diode-pumped solid state laser emitting pulses of $480-1250\,\mathrm{ps}$ duration at a repetition rate of $40-200\,\mathrm{kHz}$, resulting in an average power of $0.84-2.28\,\mathrm{W}$. The lasers are both mounted to the upper optical breadboard (Figures 6, 7). After exiting each laser and passing through a series of fold mirrors, the beams are expanded and collimated by a pair of $2\mathrm{X}-8\mathrm{X}$ beam expanders (Edmund 87-567) before they are joined by a 25 mm polarization beam combiner (Edmund 86-710). The combined beam is then guided by a pair of periscope mirrors down to the scanning subframe, which is suspended from the upper optical breadboard. The complete alignment of each laser and the coalignment of the two lasers followed the procedure described in last year's report, Project Report LSP-181.

The scanning subframe (Figure 8a) supports the dual-axis galvanometer scan head and the focusing optics (Figure 8b). The galvanometer scanner consists of two mirrors mounted on orthogonal shafts that are each connected to an electromechanical actuator. Because the relative position of the galvanometer scan head to the focusing optics is critical, the fixture holding the mirrors is mounted to a precision 3-axis linear stage (Newport 562-XYZ). In response to two analog voltage inputs, the actuators rotate the mirrors, deflecting the beam in the x-direction and the y-direction. The beam then passes through an F-theta lens, which focuses the beam onto the build plane over a square, planar area. The depth of focus was calculated to be about $4\ \mu\mathrm{m}$. The length of the build area in a given coordinate direction is simply the product of the focal length of the F-theta lens ($f = 100$ mm) and the total scan angle of the galvanometer ($\theta = 40°$), or about 70 mm.

2.1.2 Build chamber

A modular aluminum box with bi-fold doors surrounds the lasers, optical components, and build platform, acting as both a build chamber and a secure safety enclosure (Figure 6). The power supplies and controllers for the lasers and galvanometer scanner are located outside the box. The frame of the box is constructed from aluminum T-slot rails, and the doors and panels are 0.125-inch 6061-T6 panels. Holes were cut in the panels to allow for purging the box with inert gas and the pass through of cables for power and control. The box allows convenient access to all components of the micro-SLM through the doors, and it can also be lifted off the lower optical breadboard or partially disassembled when further access is required.

Metals must be fused in a protected, inert environment in order to prevent contamination and minimize oxidation that causes defects in the fused material. Because exceptionally high vacuum is required to prevent oxidation of many metals, selective laser melting is conducted in a sealed chamber filled with high-purity nitrogen or argon gas. Provisions were therefore made to seal the box and purge it with argon gas. Gaskets were installed, holes and gaps in the panels were taped or plugged with foam inserts, and an exhaust vent with an oxygen sensor was added.
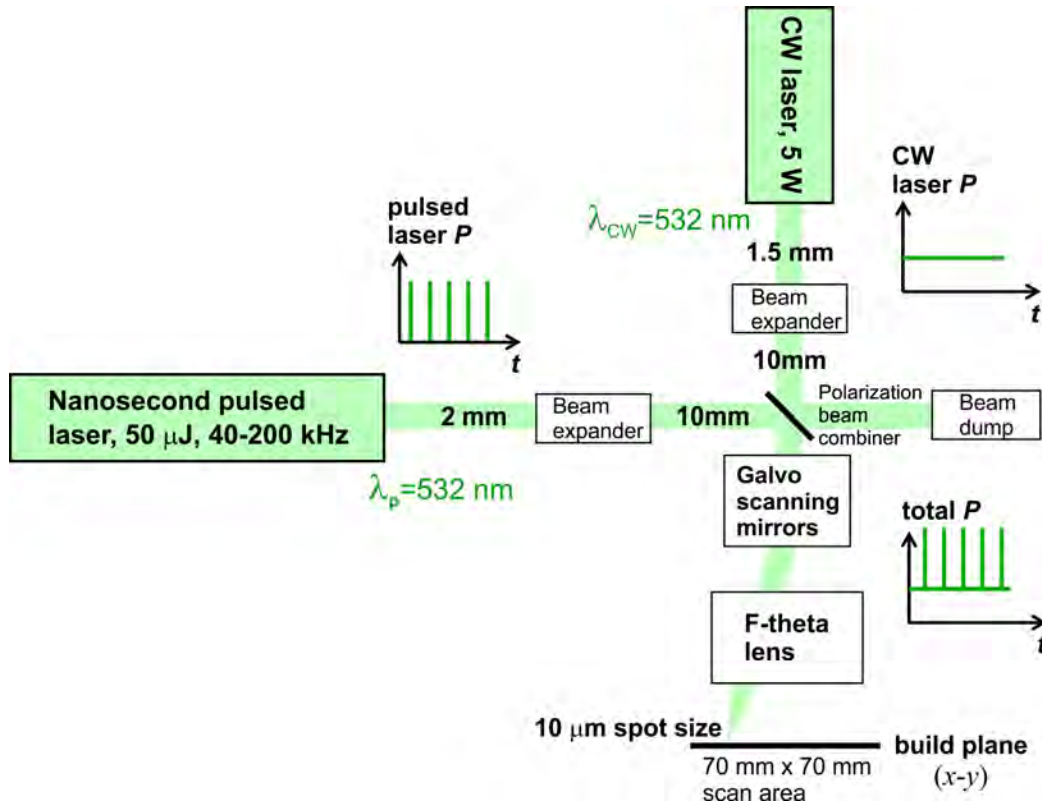
Figure 5. The beams of the continuous wave (CW) laser and pulsed laser combine to form a single beam with spot size $d_{\text{beam}} = 10\,\mu m$ at the build plane. The combined beam therefore can have both a mean component and an oscillatory component. (Actual system is three-dimensional, with the build plane below and parallel to the plane that contains the lasers.)

The second purpose of the aluminum box is to protect the operators and observers in the room from the hazards of laser radiation. Thus, the color of the interior surfaces of the panels of the box was specified to be matte black in order to maximize the enclosure's absorption of laser radiation, and the gaps between the panels were sealed with aluminum laser tape. A safety interlock disconnects the power to the lasers when the doors are opened. Because the lasers are securely enclosed within the box, the system can function as a ANSI/IEC Class 1 laser. A Class 1 rating allows personnel without Laser Safety Training to be in the room when the laser is turned on.

2.1.3 Build platform

The build platform consists of the build plate and the 3-axis linear translation stage (Figure 9). The build plate directly supports the sample to be fused and is most often a plate constructed from
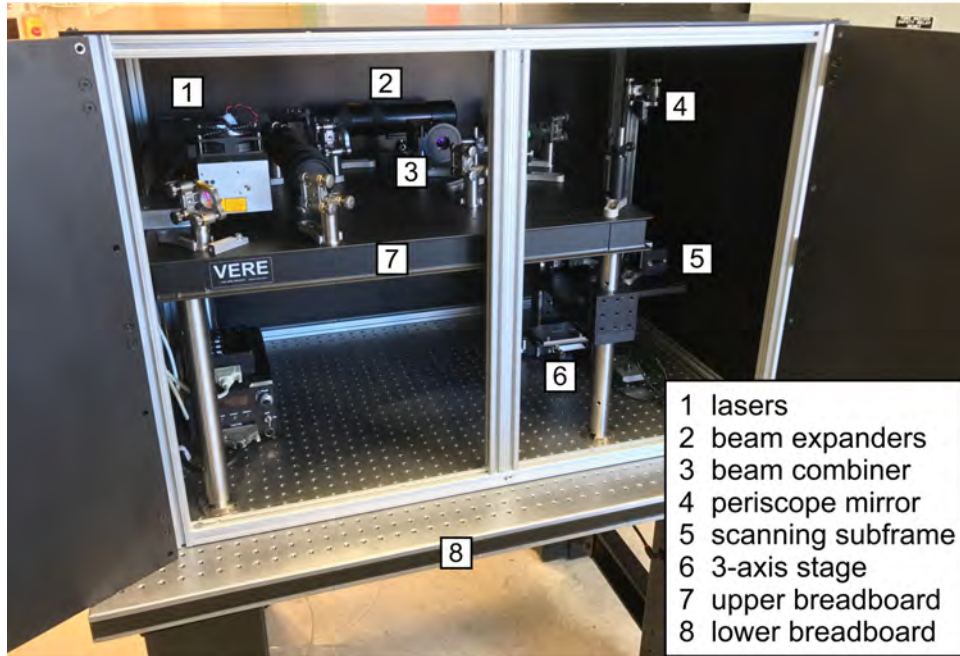
Figure 6. Photograph of the laser fusion components of the micro-SLM machine, including lasers, all optical components, support structures, and build chamber.

metal identical to that of the powder. The build plate is fastened to the translation stage by an aluminum fixture that is bolted to the y-stage. The y-stage is used only to position the sample in the build plane initially. The z-stage (Colorado Stages with precision servo) is mounted to a tip-tilt anchor that enables the build plate to be precisely aligned with the focal plane of the F-theta lens (i.e. the build plane). The integrated controller of the z-stage ensures that the top of sample is initially located at the focal length of the F-theta lens. For multi-layer, multi-material printing, the x-stage would translate the sample over to the powder recoater and the DPE printhead with submicron resolution. Between fusion of layers, the z-stage would lower the build plate by a distance equal to the thickness of the newly spread or printed powder.

2.2 CHARACTERIZATION OF LASERS

The output power of the CW laser was measured both at the laser and at the build plane with a Newport Model 1928-C optical power meter (Figure 10a). Measurements of stability showed an acceptable intensity noise of about 1% root mean square after an initial settling period of several seconds. The power at the build plane was about 30% lower than the power at the laser, indicating that significant loss of energy occurred during the transmission of the beam through the steering

10
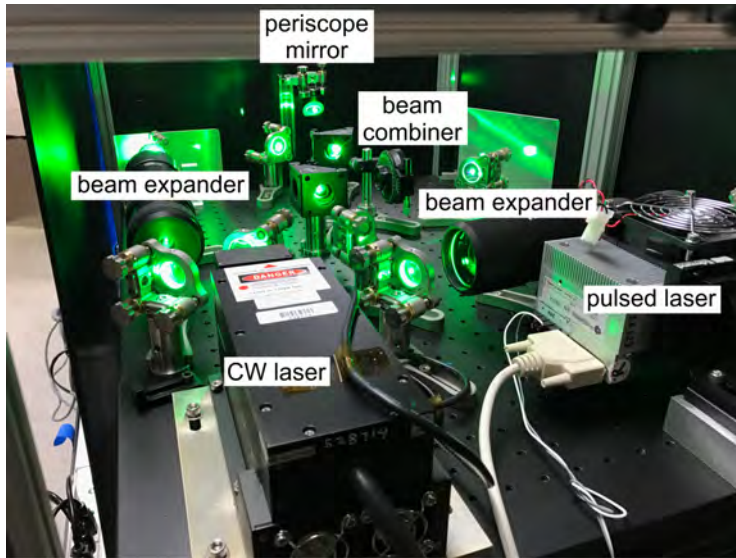
Figure 7. Photograph of the lasers and optical components located on the upper optical breadboard.

optics. These losses are typical of SLM machines and not overly concerning. However, at both the laser and the build plane, the output power did not increase linearly as the input voltage was increased, but instead it dropped and spiked sharply several times (Figure 10b). Furthermore, at a given input voltage, the output power was not the same during a ramp-up of voltage as it was during a ramp-down of voltage. These types of response would make difficult a controlled investigation of the effects of laser power on melt pool characteristics and fused material properties. The manufacturer reported that this performance is typical for this model of laser and suggested the generation of a look-up table mapping output power to command voltage. An alternative solution would be to install a pocket cell that might sufficiently modulate the laser amplitude (e.g., Thorlabs EO-PC-550).

The pulsed laser was characterized by the manufacturer and proved to be within specification. The measurements are provided in Appendix 1.

2.3 THE LASER BEAM: CONTROL OF POWER, POSITION, AND SCAN VE-LOCITY

During fusion of a sample, the power, scan velocity, and position of the laser beam at the build plane are set by a waveform control system. This system consists of electronics, software, and a computer that send analog voltage signals to the CW laser and each of the two galvanometer mirrors. The output power of the CW laser and angle of rotation of each mirror should be linearly
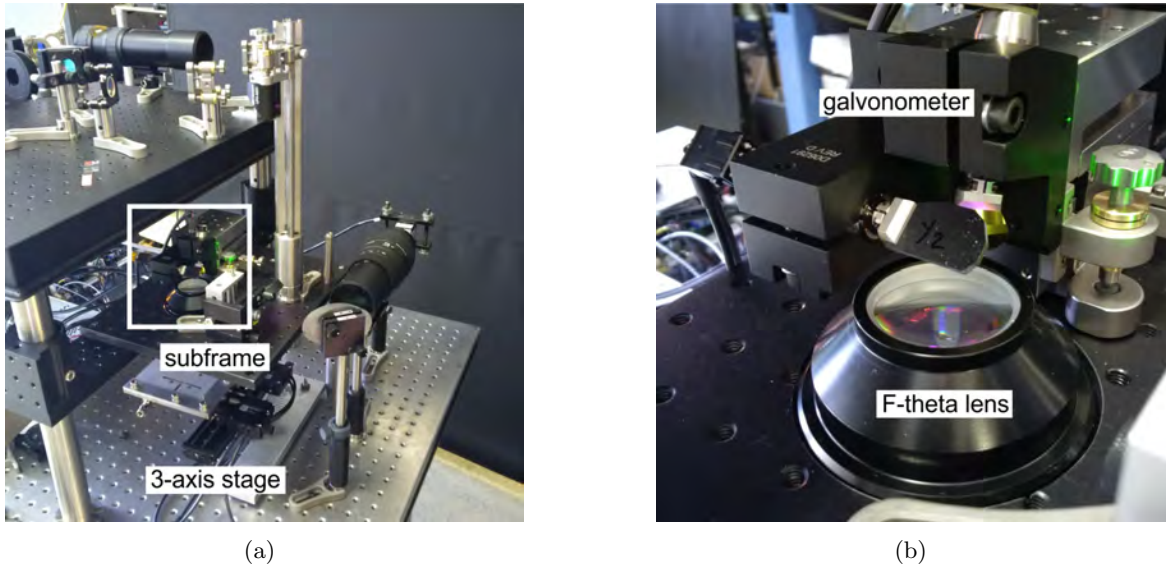
Figure 8. Photographs of optical components located on the scanning subframe: (a) Scanning subframe suspended below the upper optical breadboard; (b) Magnification of the boxed area in Figure 8a, showing the F-theta lens and dual-axis galvanometer scan head.

proportional to this voltage signal. At this time, the output power and pulse rate of the pulsed laser are set manually, but the electronics include unused channels that could be used to control its output (as well as the powder recoater, DPE printhead, and translation stages).

The input to the control system is a preprogrammed array that describes a complete scanning operation. The scanning operation consists of a sequence of laser scan paths that the system will execute in order. A scan path is defined as a movement of the laser beam between two positions that occurs with constant laser power and constant scan velocity. (If the pulsed laser were added to the control system, the average power would be constant when calculated over a time period much larger than the duration of a single pulse.) The initial array of laser powers, positions, and scan velocities is programmed in G-code, a simple programming language commonly used for the numerical control of machine tools. For initial testing of the micro-SLM, the G-code was generated manually or by a MATLAB script in the form of a text file. In the G-code, the geometry of each scan path is defined solely by the location of its start and end points.

Because only the position, not the velocity, of the galvanometer mirrors can be controlled directly, each scan path must be subdivided into many points, defined by their (x, y) coordinates. The collection of (x, y) coordinates determines the waveforms required to control the position of each mirror as a function of time. For a given scanning operation, a time interval, Δt_{step}, separating
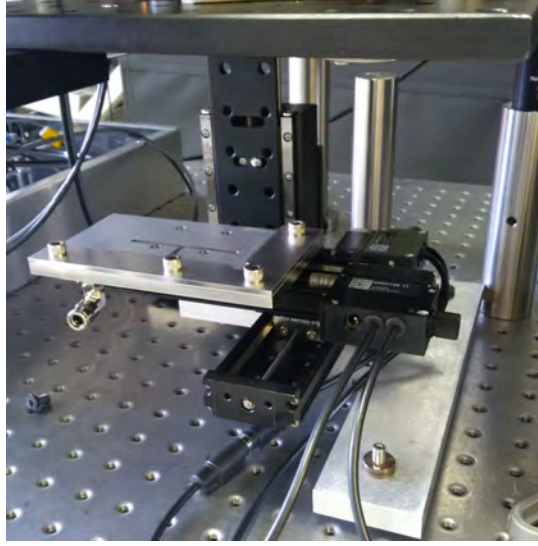
Figure 9. Low profile, 3-axis translation stage used to position the build plate and sample for laser fusion. Parallelism with the focal plane is set by a tip/tilt anchor (bottom).

each point is chosen, and the distance separating each point is calculated from the scan velocity:

$$d_{\text{step}} = v_{\text{scan}} \; \Delta t_{\text{step}}, \tag{1}$$

A Python script converts the G-code representation of each scan path into a digital waveform and writes each (x, y) position and the associated laser power to a file in comma-separated value format (CSV). A custom LabVIEW application then reads the CSV file, converts each value of power and position into its voltage representation, and sends the digital signal to a National Instruments NI-9264 voltage output module at time intervals Δt_{step}. The voltage output module then converts the digital signals into analog voltages and outputs the voltages to the laser and galvanometer mirrors.

In order to distribute the laser energy evenly along the scan path, approximating constant scan velocity as closely as possible, the time for which the laser dwells at each point (the step time) should be minimized. The minimum step time should be determined by the maximum update rate of the voltage output module, $f_{\text{max}} = 25 \, \text{kHz}$, with

$$\Delta t_{\text{step}}^{\text{min}} = \frac{1}{f_{\text{max}}} = 40 \, \mu\text{s}. \tag{2}$$

However, in the programming of the LabVIEW application, the processing of the CSV file and the method of communication with the voltage output module were not optimized. As a result, the frequency of input to the laser and galvanometer scanner was limited to less than $5 \, \text{kHz}$,
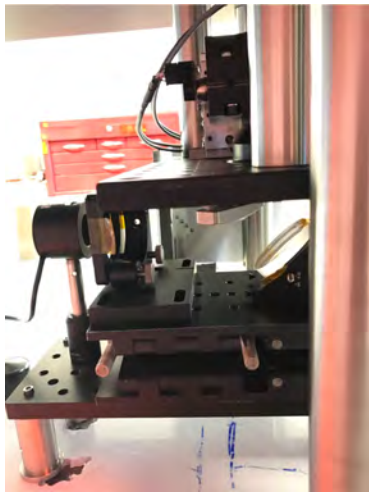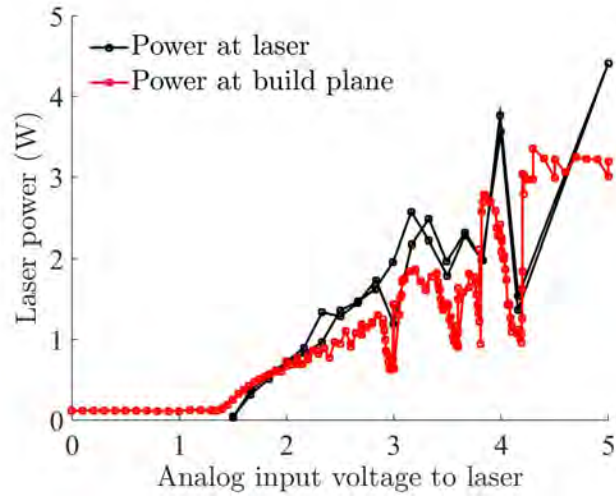
(a)   (b)

Figure 10. Characterization of the output power of the continuous wave laser: (a) Output power measurement at the build plate; (b) Output power shows several sharp dips and spikes as the input voltage is ramped up or down. (Output power at the laser was measured during both a ramp-up and a ramp-down.

causing the step time to be a minimum of $200\,\mu$s. Commercial SLM systems commonly use field-programmable gate arrays for processing and can send commands to the scanner at frequencies of up to $100\,$kHz [12].

3. METAL POWDER FEEDSTOCK: POWDER PROPERTIES, POWDER BED PROPERTIES, AND POWDER BED RECOATING

For a feedstock, the micro-SLM requires thin, homogeneous layers of fine metal particles that are tightly packed. Not only do thin layers and small particles improve print resolution, but they are necessary to ensure adequate fusion between layers. The laser must be able both to melt fully the current layer and to penetrate into previously fused layers. Because the depth of laser penetration and the depth of the melt pool are proportional to the spot size of the laser beam, the layer thickness must scale with the diameter of the beam. Furthermore, for optimal recoating results, Fischer et al. showed experimentally that the average particle diameter of the powder can be no larger than one-half of the layer thickness [3]. Because the beam diameter of the micro-SLM is $10\,\mu$m, each layer of powder should be no thicker than $10\,\mu$m, requiring powders with an average diameter of less than $5\,\mu$m. In order to form high quality powder beds from these fine particles, both the powder properties and the methods of depositing and recoating the powder bed should be optimized.

The properties of the fused material depend strongly on the properties of the starting powder feedstock. In order to minimize the porosity and surface roughness of the fused material, the uniformity and packing density of the powder bed should be maximized. Variations in layer thickness, packing density, and distributions of particle size or shape can destabilize the melt pool. These instabilities frequently lead to discontinuous or rough melt tracks that cause porosity, weak interlayer bonding, and poor surface finish. Increasing the packing density improves the thermal conductivity of the powder bed, promoting uniform heating and reducing vaporization that can cause loss of alloying elements and the formation of large pores (keyhole pores). Furthermore, with increases in packing density come also decreases in the consolidation strains that accompany melting and increases in the load bearing capacity of the unfused powder, thereby reducing residual stresses and part distortions.

3.1 PROPERTIES OF THE FEEDSTOCK POWDER

Powder bed properties are determined in part by the properties of the powder itself. The maximum theoretical packing density of a powder is determined by its distributions of particle size and shape. For a given particle shape, broadening the distribution of particle sizes increases the theoretical packing density, but, even with a distribution of sizes, powder beds with packing densities greater than 0.6 are rarely attained. The property that limits packing density is the ease by which the powder flows when spread over the build plane by the powder recoater blade or roller. Flowability is maximum for smooth, spherical particles and decreases with decreasing particle size. As the particle size decreases, the specific surface area of the powder increases, and the magnitude of adhesive and cohesive forces, including van der Waals and electrostatic forces, increases relative to both the inertia of the particles and the magnitude of the external forces applied by the recoater. Therefore, fine powders, those with an average diameter of less than about $d_{50} = 10\,\mu$m, tend to

stick to the recoater and agglomerate, causing spreading of homogeneous layers to be difficult. When standard recoating methods are used, the packing density of fine powders is only about 30 %, and the porosity of the fused material is typically high.

Considering the challenges associated with depositing fine particles, we begun efforts to determine and quantify experimentally the powder characteristics and recoating methods that would contribute to the formation of dense, uniform powder beds. For flowability and fusion experiments, we used a gas atomized, 316L stainless steel powder. Gas atomization is commonly used to manufacture powders for powder bed fusion because it produces reasonably spherical particles at an affordable cost. Supplied by TLS Technik (Germany), the powder has an average particle diameter of $d_{50} = 8.42\,\mu$m, with 80% of the mass of the powder exhibiting diameters in the range $5.2-12.09\,\mu$m. Scanning electron microscope images of the powder show that occasional large or misshapen particles exist (Figure 11a). Furthermore, not perfectly spherical, the particles display flat spots that increase rolling resistance and reduce flowability (Figure 11b). Investigating powders from other suppliers and produced by a different method, such as plasma atomization, is recommended.

(a) (b)
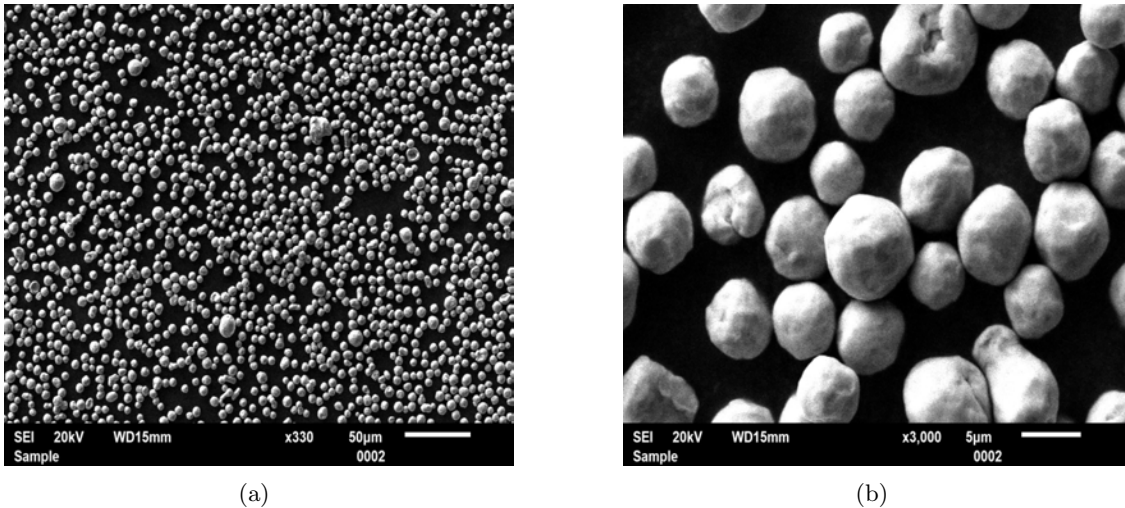
Figure 11. Scanning electron microscope images of the gas atomized 316L stainless steel powder used in the powder fusion experiments: (a) The powder shows occasional large and rod-shaped particles; (b) Particles are not highly spherical and exhibit flat spots that increase rolling resistance and reduce flowability.

For initial assessment of powder flowability and power bed surface roughness, we manually spread thin layers of the 316L powder and measured the layer's surface topography. The powder was raked across a glass slide with a razor blade offset from the surface of the slide by shim

16

stock, forming a layer of powder about $50\,\mu m$ thick on average. Grayscale images of the surface of the powder were acquired with a digital microscope, and MATLAB was then used to construct three-dimensional representations of the surface topography from the intensity of each pixel in the image. (Light pixels are higher than dark pixels because they reflect more light.) The results of these experiments show the layer thickness to be reasonably uniform but rough in texture, with a surface roughness equal to nearly half the thickness of the layer (Figure 12). Powder flowability and packing under these conditions were therefore judged to be poor, presumably due to interparticle friction and cohesive forces. However, for future experiments of this type, we recommend raking the powder over a plate of metal with a surface roughness at least as large as the average particle size of the powder in order to promote adhesion of the powder to the plate and simulate more closely the recoating process.

Because packing density and flowability are functions of the sphericity and surface roughness of the particles, efforts were also made to quantify the morphology of individual particles. Smooth, spherical particles flow and pack better than particles of any other shape. However, the appropriate length scale at which to specify smoothness is not clear. At the macroscale, flat spots on particles increase rolling resistance, but, at a microscale, surface asperities decrease contact area, strongly reducing cohesive forces and therefore the tendency of particles to cluster. The surface morphology of individual particles can be characterized with nanometer resolution by optical profilometry or atomic force microscopy. Optical profiles of individual particles were measured with a Zygo NewView 5000 surface profiler. For example, Figure 12b illustrates that the surface of a highly spherical titanium particle exhibits significant surface roughness at the microscale.

(a)   (b)
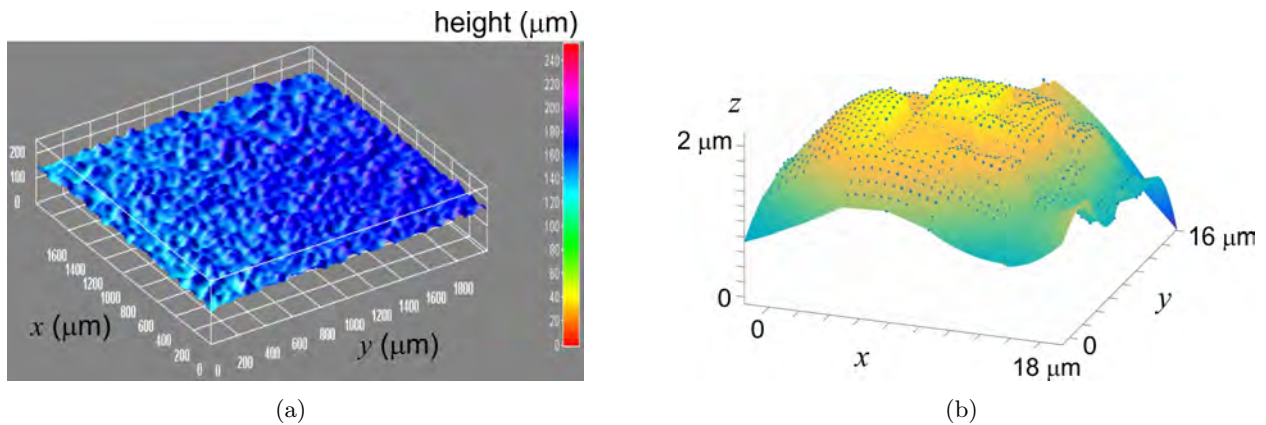
Figure 12. Optical measurement of the properties of the powder bed and powder particles: (a) Surface roughness of a manually spread layer of 316L stainless steel powder ($d_{50} = 8.42\,\mu m$) is nearly half the layer thickness of $50\,\mu m$, indicating that particles agglomerated during spreading; (b) Surface topography of a single titanium particle shows that surface roughness exists also at the microscale ($\gtrsim 100\,nm$), potentially having strong effect on the cohesion of the particles.

17

3.2 POWDER BED RECOATING

The density and uniformity of the powder bed are determined not only by the properties of the powder particles but also by the method of spreading (recoating) the powder. In powder bed fusion systems, the powder is supplied to the build plane either from above by a hopper (Figure 1) or from below by a cylinder filled with powder. Simultaneously or afterward, the powder is evenly spread across the build plane by a doctor blade, flexible wiper, or counter-rotating rotor. The relationship between the final properties of the powder bed and the techniques and parameters for spreading the powder have not been sufficiently researched. However, there is mounting evidence that parameters such as the velocity, geometry, height, and surface texture of the recoating device can have substantial impact on the properties of the powder bed.

A simple, yet versatile, powder bed recoater, was designed and built both for use in the micro-SLM and for investigation of the effects of spreading parameters on the properties of the powder bed (Figure 13). The recoater consists of a 3-axis stage for positioning the sample, a blade for spreading the powder, an adjustable blade holder, and a motorized translation stage that moves the sample relative to the blade (Table 2). Initially, the build plate is positioned in line and before the recoater blade by manually adjusting the 3-axis stage in the x-direction and y-direction. The edge of the blade is first adjusted parallel to the build plate, and then the angle of inclination (rotation about the y-axis) and the height of the blade are set. Next, powder is deposited onto the build plane, and the motorized stage translates the blade at constant velocity in the x-direction, causing the powder to be spread evenly across the build plane. Henceforth, the x and y stages are left in place, and, after fusion of each layer, the z-stage is lowered by a distance equal to the thickness of the next powder layer before another layer is spread. Although it was completed and shown to function, the recoater was not used because of concerns from Environmental Health and Safety about the handling of fine metallic particles in the room containing the micro-SLM.

The recoater provides a platform for a thorough study of powder recoating parameters. Powders can be repeatedly spread with blades of different materials, edge geometries, and inclinations. The velocity of the blade and its separation from the build plane can be varied as well. Furthermore, provisions were also made for the addition of a DC motor and geared shaft that would enable the blade to be swapped for a counter-rotating rotor, significantly changing the nature of the powder flow. Other potential modifications include the addition of a mechanical compaction step to increase the packing density of the powder after recoating occurs. Systematic variation of recoating parameters, recoating techniques, and the properties of the powder would be followed by characterization of the resulting powder bed density and uniformity. The results would identify the parameters and properties that are correlated with the formation of dense, homogeneous powder beds.

18
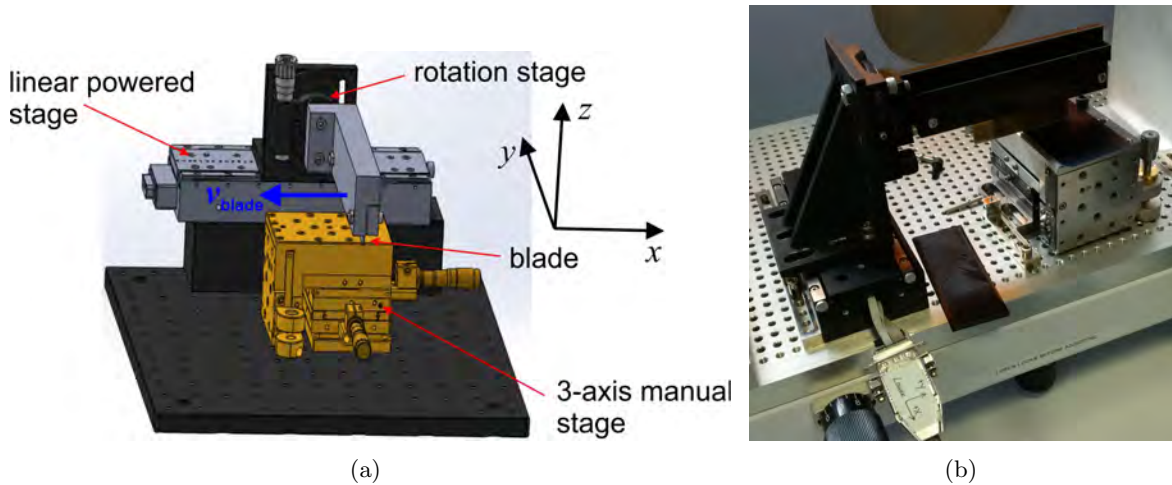
Figure 13. Design and construction of a blade-type powder recoater for (1) use in the micro-SLM and (2) investigating the impact of powder properties and spreading parameters on the density and uniformity of the powder bed: (a) Computer model of the recoater, illustrating its major components and function; (b) Photograph of the completed, functional recoater.

TABLE 2

Major Components and Key Specifications of the Micro-SLM Powder Recoater (Hopper that would store and deposit powder not included)

Component/Function	Manufacturer	Model	Specifications
Spreading blade	Alpha Knife, other	custom	variable geometry and stiffness
Blade rotation	Thorlabs	CR1/M	$\theta = 360°$, 3 mrad resolution
Spreading stage	Applied Scientific	LS-100	100 mm travel, $v_{\max} = 1.6$ mm/s
Blade holder	McMaster, custom		h=20 mm, L=80 mm
Platform positioning	Newport	562-XYZ	13 mm travel, $< 100\,\mu$rad dev.

This page intentionally left blank.

4. SINGLE TRACK MELTING TRIALS: LASER WELDING AND LASER FUSION OF STAINLESS STEEL

The performance of the micro-SLM system was evaluated by conducting two types of experimental trial: welding of stainless steel plates and fusion of stainless steel powder. In both cases, the micro-SLM demonstrated the ability to produce stable melt pools and smooth, uninterrupted melt tracks. During multi-layer builds, the micro-SLM would perform both types of fusion simultaneously as it (1) fuses the most recently spread layer of powder, and (2) fuses this layer to the layer(s) below by remelting previously solidified layers. Therefore, taken together, these experimental results indicate that the micro-SLM would be capable of fusing multi-layer samples of stainless steel or other metals with similar thermal conductivity and melting temperature.

4.1 LASER WELDING OF STAINLESS STEEL PLATE

In the first type of experiment, laser welding of 316L stainless steel plate was conducted with the CW laser and the pulsed laser operating simultaneously. Each 3.2 mm thick plate was first cleaned with isopropyl alcohol and mounted on the x translation stage. The z-stage was positioned so that the top of the steel plate was in the focal plane of the F-theta lens, resulting in the minimum laser spot size, $d_{\text{beam}} \approx 10\,\mu\text{m}$ and peak laser intensity. Both lasers were turned on at full power, and the pulse repetition rate of the pulsed laser was set to 80 kHz. Accounting for a power loss of 30% within the beam steering optics, the average laser power was therefore about 5 W at the build plane, corresponding to an average laser intensity of about $6 \times 10^6\,\text{W/cm}^2$. The x-stage was then moved a distance of 25 mm for a range of velocities at y coordinates separated by 1 mm. At a stage velocity of 5 mm/s, the combined laser beam melted a track 20 μm wide, which then resolidified into a uniform, continuous weld bead (Figure 14a). Including the weld bead, the beam created a total heat-affected zone about 50 μm wide.

In another welding test, under otherwise identical conditions, the sample was held stationary for a period of 10 s. During this time, sufficient energy was input to raise the temperature of the metal above its boiling point, causing ablation to occur. The ablation is manifested by the formation of a crater in the sample with diameter and depth of about 25 μm (Figure 14b). At the edge of the crater, material that was ejected from the hole resolidified to form a lip about 25 μm in height. It is well known that metals typically start to evaporate at a laser intensity of about $3 \times 10^6\,\text{W/cm}^2$ [6]. Furthermore, during each pulse, the pulsed laser provided a much higher laser intensity of about $6 \times 10^{10}\,\text{W/cm}^2$, which, for a nanosecond pulse duration, is in the range of processing conditions appropriate for laser drilling [8]. At this intensity, the interaction of the laser radiation with the metal vapor is surely to cause a plasma to form. The plasma expands and flows away rapidly from the melt pool, exerting both a high recoil pressure and a strong drag force on the melt pool, causing the liquid metal to be ejected from the hole.
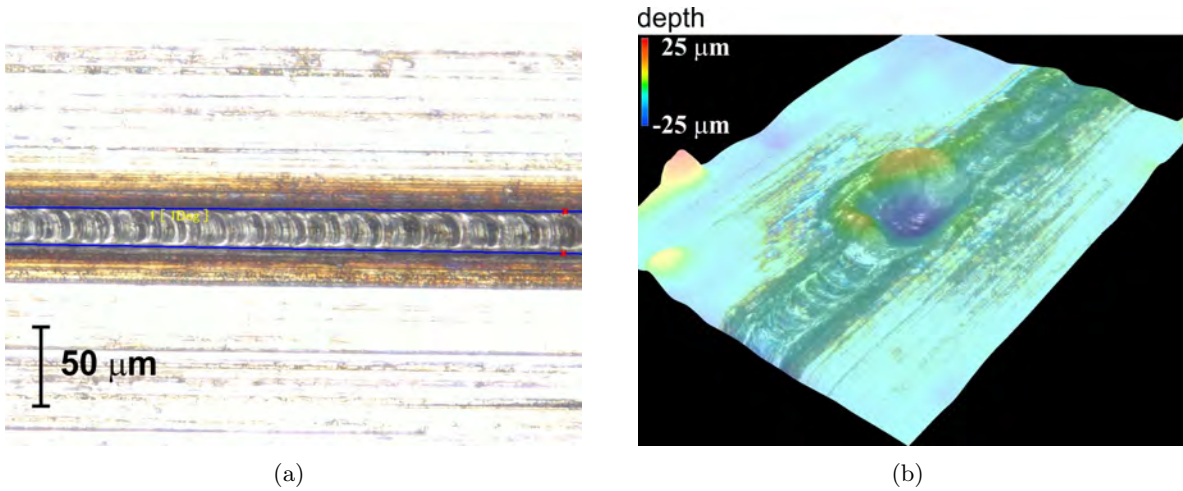
Figure 14. Weld bead in 316L stainless steel plate formed by combined continuous wave and pulsed laser beams: (a) At an effective scan velocity of 5 mm/s, the weld bead measures about 20 μm wide, and the width of the heat-affected zone is about 2.5 times the width of the weld bead; (b) When the position of the beam on the sample is fixed, ablation and ejection of material occur, causing a crater to form (laser drilling).

4.2 LASER FUSION OF STAINLESS STEEL POWDER

In the second type of experiment, successful fusion of 316L stainless steel powder was demonstrated with just the CW laser. Described previously in Section 3.1, this powder has an average particle diameter of $d_{50} = 8.42 \, \mu$m. Because the powder recoater could not yet be used due to the concerns about the safe handling of fine particles, the samples were produced manually in a fume hood. About 8 g of powder was scooped into a shallow steel cup. The surface of the powder was smoothed and flattened, and then the powder was lightly compacted mechanically to a depth of 3 mm. The waveform control system was programmed to scan a 2×3 array of sets of 10 parallel tracks (Figure 15a). The scan tracks were each 2 mm long, and within each set, tracks were separated by a distance of 160 μm. (The distance between each set of tracks was a minimum of 500 μm.) Within each set, the power setting of the laser was held constant and the scan velocity was increased from 1.2 mm/s to 12 mm/s in increments of 1.2 mm/s. The nominal laser power was increased linearly from 40% of full power for the first set to 90% of full power for the last of the six sets $(0.7-3.2 \, \text{W}$ at the sample per Figure 10b).

Each set of scan lines at constant nominal power did not produce separated single tracks but instead fused the powder into a coupon sample measuring 2 mm × 1.5 mm. At nominal powers lower than 3.5 W, the samples were fragile and broke apart when we attempted to remove them from the powder bed. Along the path of the scan lines, fusion occurred by melting, but the material was porous and weak between scan lines because fusion occurred only by partial sintering at these

22
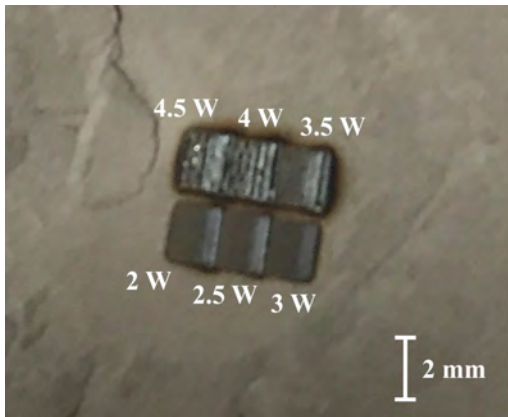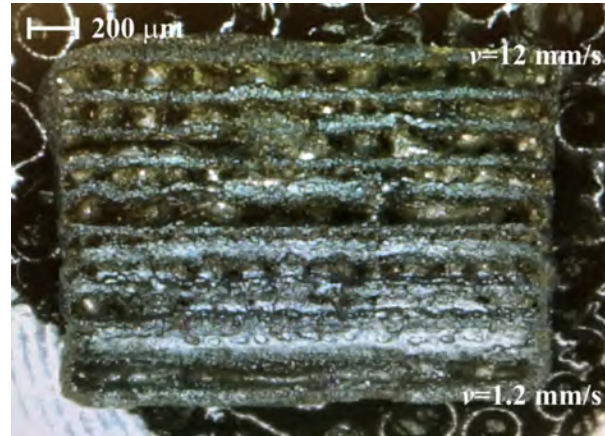
(a)   (b)

Figure 15. Rectangular coupon samples, each measuring about $2\,\text{mm} \times 1.5\,\text{mm}$*, were fused from a deep powder bed of 316L stainless steel powder (*$d_{50} = 8.42\,\mu m$*): (a) Six fused samples in a* 2×3 *array lying on the powder bed, each scanned ten times by the laser at constant nominal power; (b) Optical microscope photograph of the sample fused at a nominal laser power of 4 W, showing deep fused channels at the locations where the laser scanned, separated by material fused with a combination of sintering and melting.*

locations. For powers greater than 3.5 W, however, large melt pool volumes and a high rate of heat flow through the powder bed caused each sample to consolidate into a single piece that could be handled with tweezers. The results with a nominal laser power of 4 W are typical and illustrative of the results at higher powers (Figure 15b). At the location of each track, the fully consolidated sample exhibits a channel, about $50\,\mu$m deep, with fused material at the bottom and sides of the channel (Figure 16). Three factors may have caused the formation of these channels:

1. *Consolidation.* Although the powder was mechanically compacted gently, its packing density was likely still low—surely no higher than 0.5. Thus, the volume of the melt pool was only about 50% of the bulk volume of the powder, and gravity pulled the melt pool down into the powder bed.

2. *Ablation.* The high energy density of the laser beam, combined with the poor conductivity of the powder bed, caused the melt pool temperature to reach the boiling point. Some material simply evaporated. Furthermore, the rapidly expanding vapor exerted pressure on the melt pool (recoil pressure), pushing the melt pool down further into the powder bed.

3. *Denudation of the powder bed.* The intense flow of vapor away from the melt pool associated with ablation caused particles to be pulled into the melt track and ejected vertically. The width of denuded zones can be up to 10 times the diameter of the laser beam [4]. (The

23

wetting of unmelted particles and the associated capillary forces also pull particles into the melt pool.)

(a)   (b)
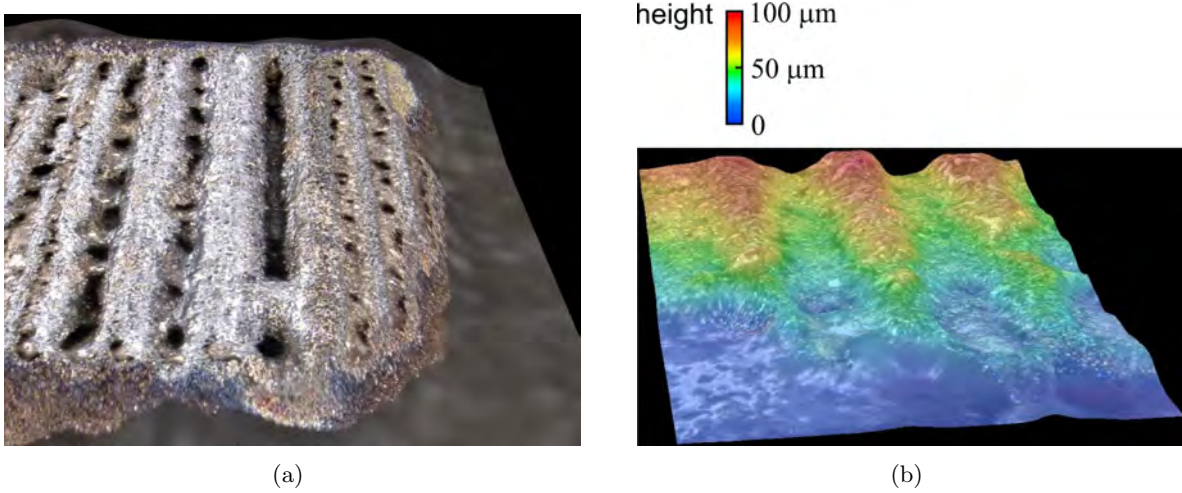
Figure 16. Fusion of 316L stainless steel powder with laser power $P = 4$ W and scan velocity $v = 1.2–12$ mm/s: (a) Three-dimensional topography of fused sample computed with optical microscope.; (b) Channels that formed where the laser scanned measure about $50 \, \mu m$ deep (b).

Scanning electron microscopy of the track fused at 2.4 mm/s shows a flat, wide track and evidence of denudation and defects (Figure 17). The surface of the track exhibits the flat shape characteristic of laser fusion at high energy densities. High energy densities flatten the melt pool both by causing large recoil pressures and by preventing the development of temperature gradients sufficient to initiate Marangoni convection (convection driven by spatial variation of surface tension). The width of the track is about $70 \, \mu m$, much larger than expected for a laser spot size of $10 \, \mu m$. Considering that the width of stable melt tracks in laser fusion is typically about twice the diameter of the laser beam, this track suggests that the spot size of the beam was at least $20 \, \mu m$. The surface of the manually compacted sample of powder was most likely neither precisely parallel to the build plane nor within the $4 \, \mu m$ depth of focus of the optics, causing the spot size of the beam to increase. The many unmelted particles scattered on and near the fused track confirm the occurrence of denudation (Figure 17a). Furthermore, at locations where the laser paused between steps, we see many cracks normal to the direction of the maximum temperature gradient (Figure 17b).

With increasing scan velocity, the fused tracks become discontinuous and increasing rough (Figure 15b). Discontinuity of a melt track indicates that the stability of the melt pool was
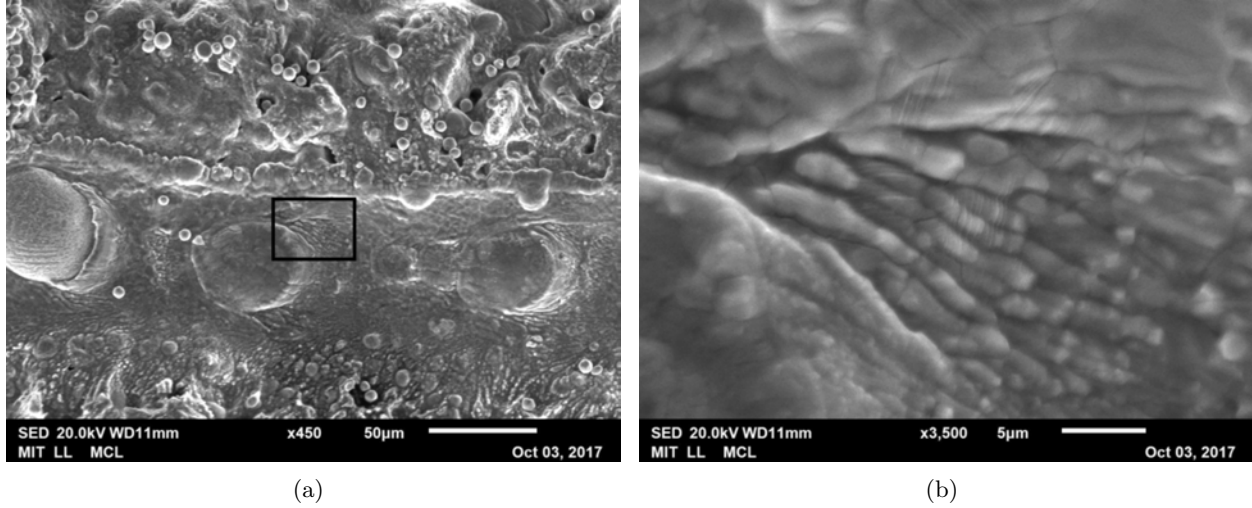
Figure 17. Scanning electron microscope images of the track fused with laser power $P = 4\,\mathrm{W}$ and scan velocity $v = 2.4\,\mathrm{mm/s}$: (a) The high energy density caused flat, wide tracks to form; (b) Cracks in the fused material developed normal to the direction of maximum temperature gradient (magnification of the black box in Figure 17a).

perturbed. As a result, the melt pool adopts the shape that minimizes its ratio of surface area to volume, i.e., a sphere, commonly known as "balling." In the regime of low scan velocities, balling is caused by oxidation, high powder bed porosity, and excessive melt pool volumes, all of which were likely present in these trials. Even so, the apparent occurrence of balling only at the higher scan velocities is somewhat surprising. The nominal energy density, $E_{\mathrm{A}} = P/\left[v \cdot d\right]_{\mathrm{beam}}$, decreases with increasing scan velocity, generally leading to melt pools of smaller size and shorter duration that are less likely to break apart than are melt pools formed at higher energy densities.

However, in our experiments, the increase of scan velocity increased nominal energy density E_{A} but did not significantly affect the temperature of the powder bed. For a given ratio of laser power to beam diameter, the increase in temperature of the material is nonlinearly related to $\left[v \cdot d\right]_{\mathrm{beam}}/\alpha$, in which α is approximately the thermal diffusivity of the powder (derivation given in Section 5). For $\left[v \cdot d\right]_{\mathrm{beam}}/\alpha \lesssim 0.1$, virtually no change in temperature occurs with decreasing scan velocity because the heat flow has nearly reached steady state. In these fusion trials, steady state heat flow should have occurred at all scan velocities. Balling at the higher scan velocities may have been caused by the accumulation of heat in the powder bed. (Powder is a good insulator). The separation of the tracks was smaller than the characteristic diffusion distance, $L_{\mathrm{d}} \sim \sqrt{\alpha\,t}$. Future fusion trials should be conducted at higher scan velocities and with increased spacing between tracks.

The brief exploration of material morphology of this section demonstrates clearly that the process parameters and processing conditions of the micro-SLM require further development. For laser scan parameters, we recommend higher scan velocities, shorter dwell times, and larger spatial overlap of steps. Further trials were not conducted in FY 2017 because of the concerns about the safety of handling fine powders in the space where the micro-SLM was located.

5. MATHEMATICAL MODELING OF LASER MELTING

Analytical modeling and a scaling analysis of the laser heating process were conducted for the purpose of planning experiments, interpreting experimental results, and determining process parameters. The specific goals of this effort were to estimate the temperatures and dimensions of the melt pool and to determine how these characteristics are related to process parameters, such as laser settings and material properties.

5.1 DERIVATION OF ANALYTICAL MODEL AND SCALING RELATIONS FOR LASER HEATING

The laser beam, with radius r, moves at constant velocity v in the x-direction as it scans over the surface of the powder bed, which lies in the (x, y) plane (Figure 18). The powder bed is modeled as a semi-infinite body and the laser beam is represented by a Gaussian intensity distribution in the (x, y) plane,

$$I(x, y, t) = \frac{A \cdot P}{\sigma \, \pi \, r^2} \exp\left(-\frac{(x - v\,t)^2 + y^2}{\sigma \, r^2}\right) \equiv I_0 \exp\left(-\frac{(x - v\,t)^2 + y^2}{\sigma \, r^2}\right), \tag{3}$$

where P is the power of the laser beam at the surface of the powder bed, A is the absorptivity of the powder, I_0 is the peak intensity of the beam, and σ describes the shape of the intensity distribution. Approximating the material properties to be constant and assuming that the heat transfer is dominated by thermal conduction, the heat diffusion equation can be written as

$$\rho \, c_p \frac{\mathrm{d}T}{\mathrm{d}t} - k \left(\frac{\partial^2 T}{\partial x^2} + \frac{\partial^2 T}{\partial y^2} + \frac{\partial^2 T}{\partial z^2}\right) = I(x, \, y) \, \delta(z), \tag{4}$$

where $\rho \, c_\mathrm{p}$ is the heat capacity per unit volume, k is the thermal conductivity, and $\delta(z)$ is a delta function at the surface of the powder bed.

At steady state, the heat equation can be solved for $t = 0$, when the laser beam is at $x = 0$, by superimposing the Gaussian intensity distributions that occurred at earlier times $t' = 0 \to -\infty$ when the beam was located at coordinates (x', y'). The solution is found by by a standard Green's function method and then integrated analytically over x' and y' [2]. Transformation to dimensionless variables results in

$$T(x, \, y, \, z) - T_0(x, \, y, \, z) = \frac{A \cdot P}{k \, r} \int_0^\infty \frac{\exp(-H)}{\sqrt{\sigma} \pi^{3/2} (1 + u^2)} \mathrm{d}u, \tag{5}$$

with

$$H = H\left(\frac{x}{r}, \, \frac{y}{r}, \, \frac{z}{r}, \, \frac{v\,r}{\alpha}, \, \sigma, \, u\right), \tag{6}$$
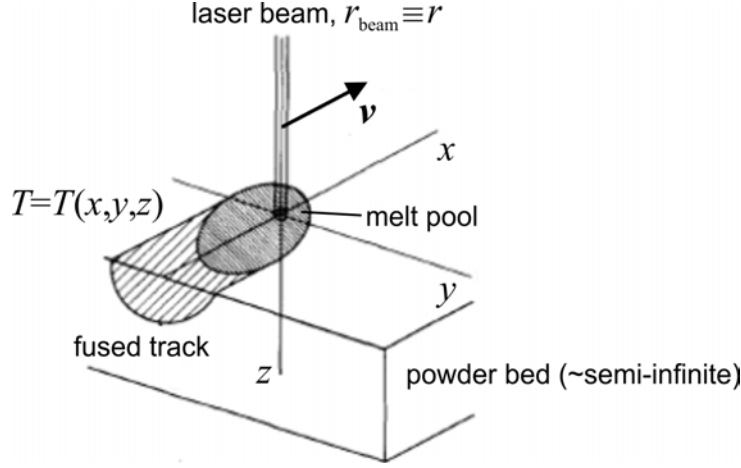
*Figure 18. Schematic of the modeling of the laser fusion process. The laser beam moves at constant velocity in the x-direction, and the powder bed is approximated as semi-infinite. The model predicts the steady temperature distribution that moves with the beam at velocity **v**.*

in which u is a dimensionless function of $t'' \equiv -t'$. The solution therefore takes the form of an amplitude term that does not vary with position multiplied by a dimensionless shape function:

$$T\left(x,\,y,\,z\right) - T_0\left(x,\,y,\,z\right) = \underbrace{\frac{A \cdot P}{k\,r}}_{\text{dimension}\,T} \times \underbrace{f\left(\frac{x}{r},\,\frac{y}{r},\,\frac{z}{r},\,\frac{v\,r}{\alpha},\,\sigma\right)}_{\text{dimensionless shape function}}. \qquad (7)$$

The amplitude term increases with increasing absorbed power and decreases with increasing thermal conductivity and beam size. The shape function, f, depends only on dimensionless velocity, $\bar{v} \equiv v\,r/\alpha$, and the shape of the beam's intensity profile. The dimensionless velocity, also known as the Péclet number, characterizes the ratio of heat flow by transport to heat flow by diffusion. For a given thermal conductivity and beam intensity, f completely determines the distribution of temperature in the material. (Similarly, a dimensionless group describing the power that is required for the laser melting of metals can be defined by dividing the amplitude term by the temperature rise: $\overline{P} \equiv \dfrac{A \cdot P}{k\,r}\dfrac{1}{(T_\mathrm{m} - T_0)}$ [7].)

We numerically integrate Equation 5 and plot the shape function along each of the coordinate axes to determine the maximum temperature in the material and explore the shape of the temperature distribution as a function of $\bar{v} = v\,r/\alpha$ (Figure 19). As expected, in the y and z directions, the temperature is a maximum at the center of the beam and at the surface of the material ($y = 0$, $z = 0$). However, in the x-direction, the maximum temperature shifts further behind the center of the beam as $\bar{v}$ increases (Figure 19a). As the beam velocity increases, the time for heat

flow by conduction decreases, and the effect of heat input at prior times and locations begins to dominate over the effect of thermal conduction.

The key result of this analysis is the nonlinear relationship between $\bar{v}$ and the distribution of temperature in the material. At constant laser intensity, when $\bar{v}$ decreases in the range of $\bar{v} = 1-100$, the maximum temperature in the material increases logarithmically, but thereafter there is little benefit to increasing $\bar{v}$. Similarly, the size of the melt pool, indicated by the width of the temperature distributions at a given value of f, does not increase significantly for $\bar{v} \lesssim 1$. This result explains the limitations in laser fusion of increasing energy density, $E_{\mathrm{A}} = P/(v \cdot 2\,r)$, by decreasing laser scan velocity. Rather, it is preferable to increase laser power, particularly for alloys with high thermal conductivity, such as aluminum alloys.

5.2 PREDICTION OF MICRO-SLM PROCESS PARAMETERS

Here, we use the results of the scaling analysis to predict the process parameters required to fuse stainless steel powder at the microscale. With the effects of dimensions removed, scaling relations are a powerful tool for the comparison and prediction of the results of experiments or processes that occur at different scales. The results of prior work conducted with lasers of different power and spot size can therefore inform our choice of process parameters.

Both Childs et al. [1] and Yadroitsev et al. [11] studied the effects of process parameters on laser fusion of stainless steel powders. They created process maps that connect beam velocity and nominal laser power to the various types of single track that can form. Using a laser with beam radius of $r = 275\,\mu\mathrm{m}$, Childs et al. found that the ideal continuous, rounded tracks occurred in a range of powers and velocities centered at about $P = 150\,\mathrm{W}$ and $v = 10\,\mathrm{mm/s}$, respectively. Using a low-power laser with a beam radius of just $r = 35\,\mu\mathrm{m}$, Yadroitsev et al. found the optimum parameters to be about $P = 25\,\mathrm{W}$ and $v = 100\,\mathrm{mm/s}$. Because the material properties, laser absorptivity, and beam shape should be about the same in the two sets of experiments, we can compare the experiments directly using the ratios of Equation 7. Although the absolute laser powers and scan velocities are very different in these experiments, the normalized powers, $P/r = 550-710\,\mathrm{W/mm}$, and the dimensionless velocities, $\bar{v} = 5.4-6.9$, are similar, as predicted by the scaling relations (Table 3).

The normalized powers and dimensionless velocities calculated from the results of prior single track fusion experiments suggest a likely processing window for the fusion of stainless steel with the micro-SLM. In the powder fusion trials of Section 4.2, the normalized power was close to this window at $P/r = 400\,\mathrm{W/mm}$, but the dimensionless velocity, $\bar{v} = 0.024-0.20$, was far too low (also in Table 3). The low velocity caused overheating of the material and an excessive volume of melt. These processing conditions are known to result in flat or concave melt tracks and densification, as we observed in our trials. Only at higher velocities do gradients of temperature and surface tension drive material flow such that optimum, rounded tracks can form [1]. Using the scaling relations, we calculate the target process parameters for the micro-SLM to be $P = 3\,\mathrm{W}$ and $v = 500\,\mathrm{mm/s}$.
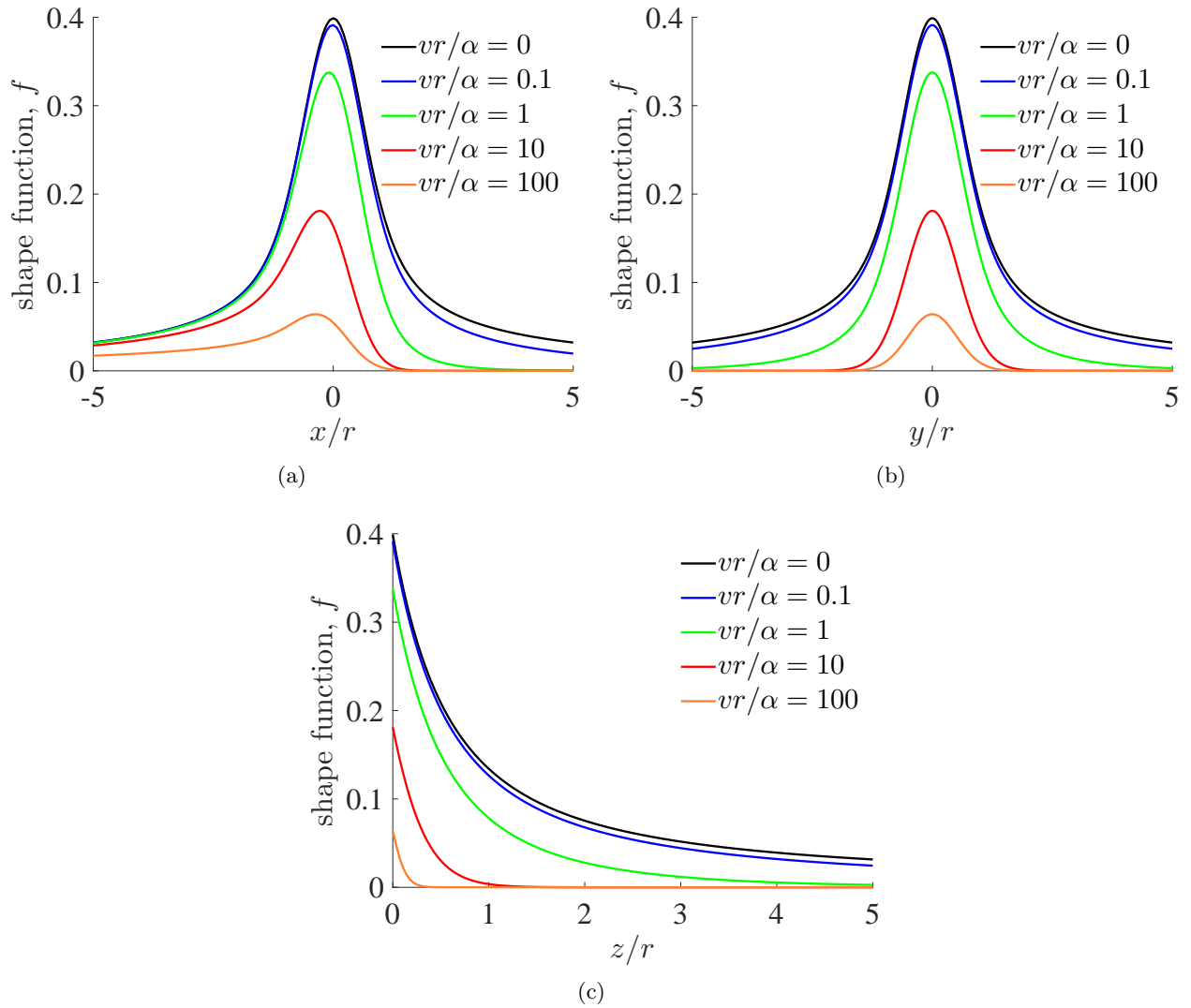
Figure 19. Plots of the shape function f that predicts the distribution of temperature in the powder bed as a function of dimensionless velocity, $\overline{v} = v\,r/\alpha$: (a) Along the x-axis, the direction of laser travel, the peak temperature lags behind the location of the beam (x = 0); (b) Along the y-axis, the temperature distribution is symmetric; (c) Along the z-axis, f predicts the depth of penetration of the temperature disturbance. As $\overline{v}$ decreases, f and thus the temperature distribution approach constant profiles.

With these target process parameters as input, predictions of the temperature field and the shape and size of the melt pool are calculated by integrating Equation 5. The maximum

TABLE 3

Use of Scaling Relations to Obtain the Micro-SLM Process Parameters from the Process Parameters Determined for Fusion of Stainless Steel by SLM at Different Scales

Experiments	Laser power	r	v	P/r	$\overline{v} = v\,r/\alpha$
Childs et al. [1]	150 W	275 μm	10 mm/s	550 W/mm	5.4
Yadroitsev et al. [11]	25 W	35 μm	100 mm/s	710 W/mm	6.9
micro-SLM Section 4.2	4 W	$\sim$10 μm	1.2-12 mm/s	400 W/mm	0.024-0.20
micro-SLM *target*	3 W	5 μm	500 mm/s	600 W/mm	5

temperature predicted, over 5000°C, exceeds the boiling point of stainless steel and indicates that vaporization will occur at the surface of the melt pool (Figure 20a). The occurence of vaporization is common in SLM and is not a concern unless it causes a signficant change in the elemental composition of the metal. The predicted melt pool measures about 40 μm long, 15 μm wide, and 7 μm deep, with the hottest and widest section of the melt pool trailing behind the center of the beam (Figure 20b). A melt pool of these dimensions is expected to be stable because it avoids the capillary instability that occurs in liquid cylinders or half cylinders with $L/d > \pi$ or $\sqrt{3/2}\,\pi$, respectively [11]. For multi-layer builds, however, the predicted depth of the melt pool (7 μm) appears problematic. The laser beam must melt both the current layer of powder and penetrate sufficiently into the previously fused layer(s) to ensure that a strong bond forms between layers. For this bonding to occur, the modeling indicates that the thickness of each layer of powder should be no greater than about 5 μm. According to the results of Fischer et al. [3], spreading uniform layers of this thickness would require the use of powders with an average diameter of less than or equal to 2.5 μm–significantly smaller than the powder used in our fusion trials and an order of magnitude smaller than the powders presently used in SLM.
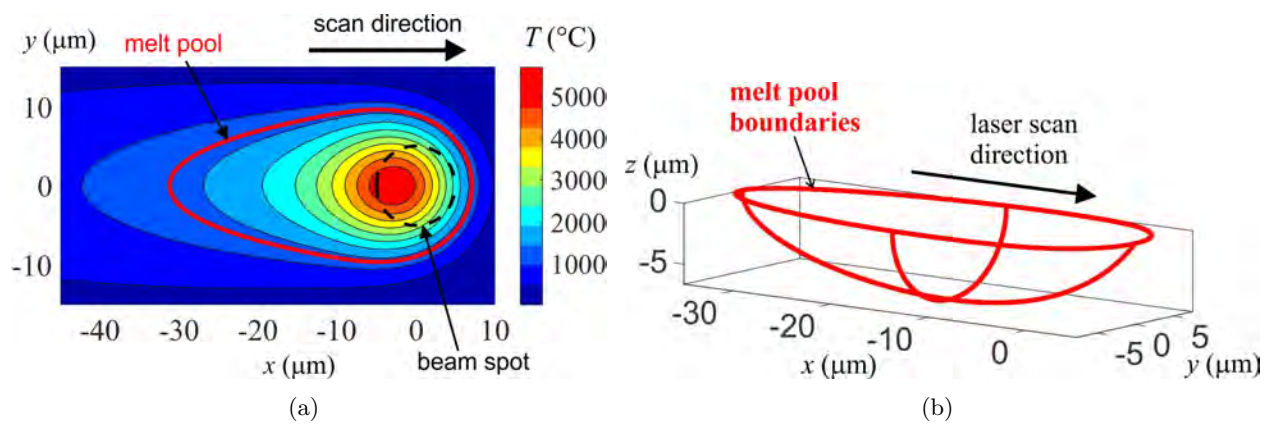
Figure 20. Model predictions of the temperature $T(x, y, 0)$ and dimensions of the melt pool for the micro-SLM target parameters, $P = 3\,\mathrm{W}$ and $v = 500\,\mathrm{m/s}$: (a) Contour plot of melt pool temperature with the shape of the laser beam and melt pool superimposed; (b) Boundaries of the melt pool in three dimensions at its maximum length, width, and depth.

6. DIGITAL PARTICLE EJECTION (DPE): DEVELOPMENT OF SYSTEM FOR ON-DEMAND, SINGLE PARTICLE PRINTING

During the past year, we have focused on the development of an experimental apparatus for on-demand electrodynamic-driven printing of single particles. The combination of high-speed control and applied electrical voltage, measurement of charge transfer during printing events, and high-speed imaging allows us to print materials on-demand while elucidating the mechanisms governing the ejection process. Accomplishments this year are summarized below and are explained further in the following sections.

1. *Automated precision experiment apparatus*
   We have automated the execution of experiments custom circuitry and a custom LabVIEW program that synchronizes all hardware components and measurements within $\sim 2 \mu$s. This has enabled us precisely quantify the dynamics of the printing process.

2. *Efforts towards understanding of single-particle ejection*
   We discovered repeatable ejection of particles that are adsorbed on the meniscus versus submerged within the droplet. This is a key physical insight for enabling robust operation of the particle printer, and the focus of our theoretical efforts. We completed our first step towards understanding the physics of particle ejection by performing a set of precision experiments characterizing the instability of liquid droplets (no particle), and discovered a scaling law for when a droplet becomes unstable; we are currently drafting a manuscript on these results.

3. *Efforts towards engineering the printhead*
   We devised a method to continuously deliver particles to the liquid meniscus at the print nozzle via a connecting inclined fluid channel. We built an experiment module to investigate feasibility of the concept, and have observed individual ejection of particles from the print nozzle with a continuous feed of particles from the channel.

6.1 AUTOMATED PRECISION EXPERIMENT APPARATUS

Our printing apparatus (Figures 21, 22) is aimed at achieving on-demand particle ejection with micron-scale precision and $\sim$ kHz rate, with fine control and measurement of the printing process based on the EHD/DPE mechanism. We have automated the experimental protocol, which comprises synchronized high-speed imaging, motorized liquid dispensing, application of voltages with programmed wave forms, and high-speed measurement of two system parameters. Typically, the measured system parameters are (1) the applied voltage, and (2) either the current from charged particles printed onto a grounded conducting substrate (Figure 21 schematic) or the pressure of the liquid at the print nozzle via an analog pressure sensor that is in fluid communication with the nozzle. (Example measurement shown in Figure 23). The protocol for an experiment is specified in advance using a custom LabVIEW program that we wrote, which then executes the protocol au-

tonomously with all measurements and hardware time-syncronized within $\sim 2\ \mu$s (Figure 23). This precise time synchronization is enabled by the PXI architecture as well as custom analog circuitry that we built for sending control signals between hardware components. Typically, camera frames and system parameter measurements are recorded at $1-10$ kHz, however we have the capability to record both at greater than 1 GHz.
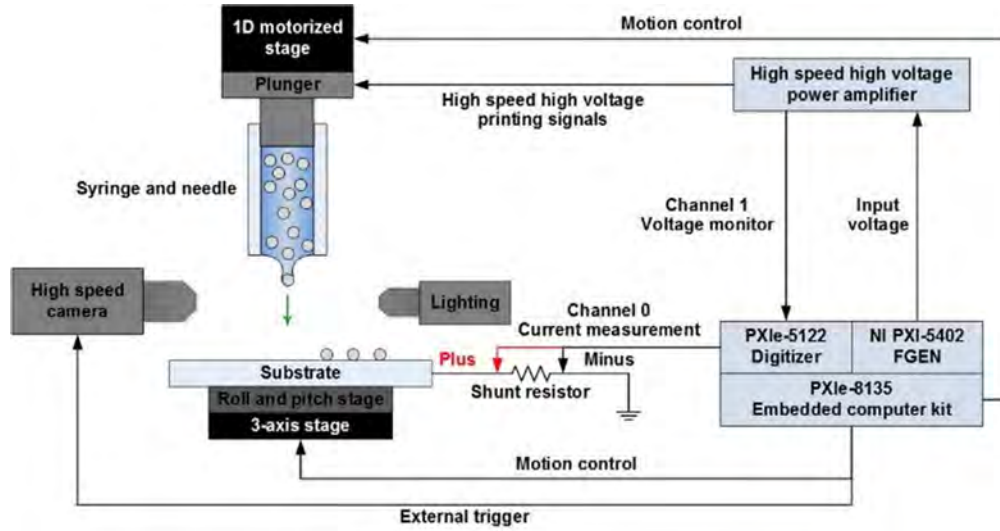
Figure 21. Schematic of the hardware and electrical connections for the printing apparatus.
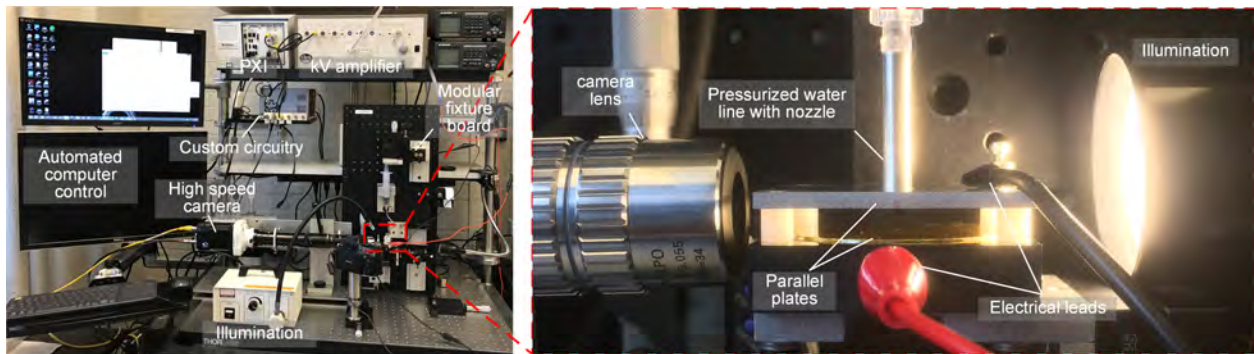
Figure 22. Image of the revised and automated experimental apparatus constructed in the Hart lab at MIT.
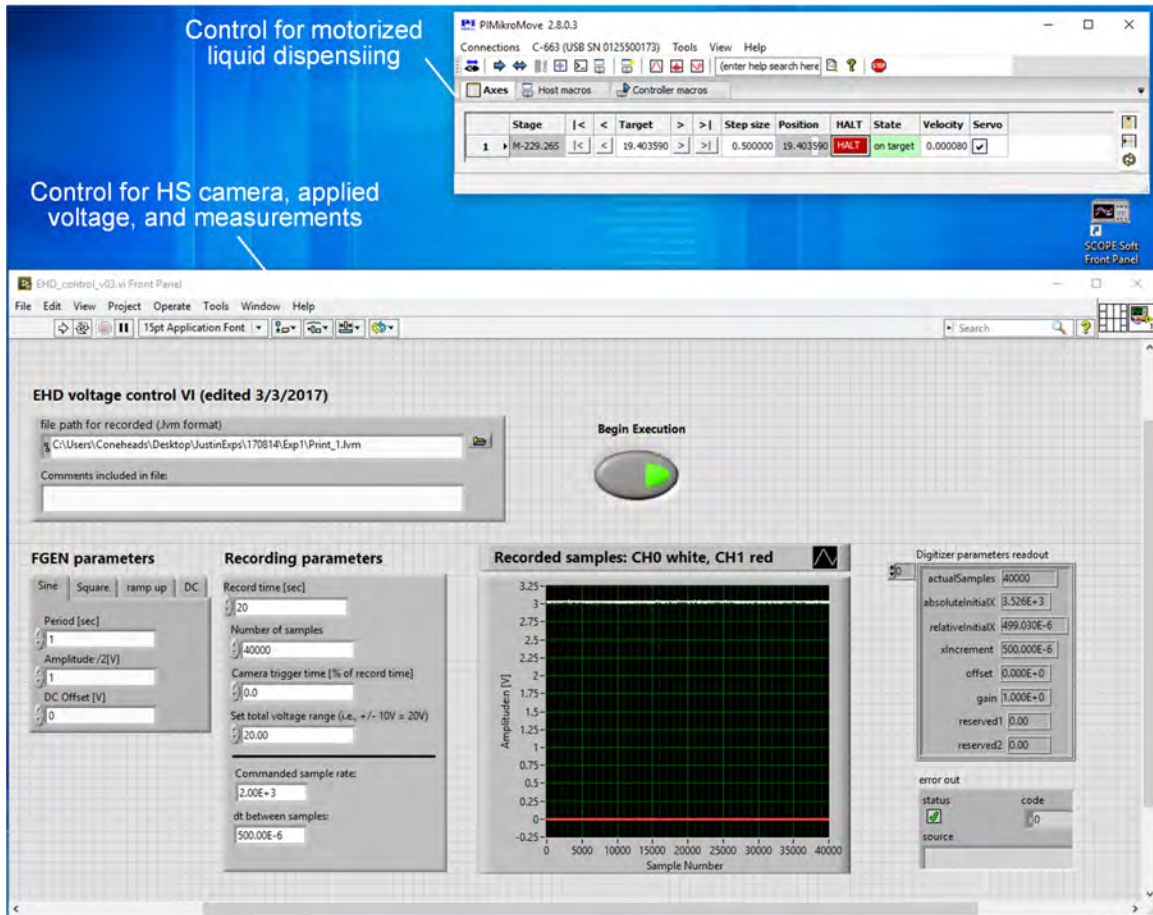
Figure 23. Front panel of our custom LabVIEW program for automated execution of experiments.

6.2 EFFORTS TOWARDS UNDERSTANDING OF SINGLE PARTICLE EJECTION

We have continued our efforts towards a rigorous understanding of the DPE single particle ejection mechanism with a combination of precision experiments and theoretical modeling. The experiment setup (Figure 25) comprises a metal needle filled with water that fits through a circular hole in the top electrode. Both the top electrode and needle are connected to electrical ground, and a bottom electrode is spaced a distance H away and held at electrical potential Φ. Our high-speed camera is focused on the liquid droplet extending from the needle to capture its dynamics when the voltage is turned on. Individual particles are put on the droplet and then a voltage pulse is applied (Figure 26). Our most important insight is that individual particles may be repeatably
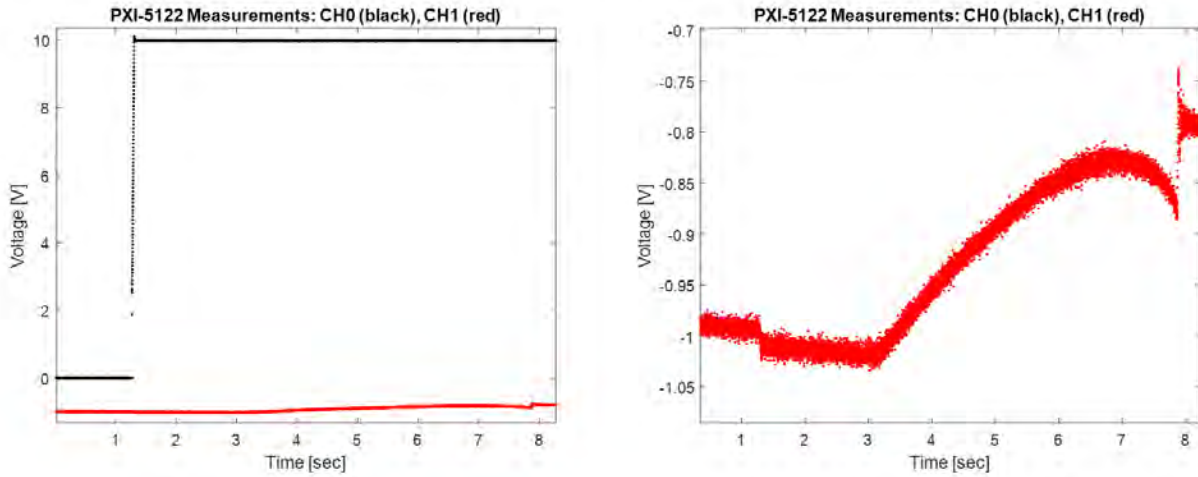
Figure 24. Example of recorded measurements of system parameters; here, the applied voltage (black, 1 kV/V) and liquid pressure (red, 1Pa/V sensitivity) are recorded. The protocol for this experiment is to apply a constant 10 kV at 1.25 seconds, and then slowly dispense liquid through the nozzle beginning at 3 seconds; the pressure of the droplet increases, and then decreases before the ejection of a particle, which corresponds to the pressure jump at about 8 seconds.

ejected from the droplet, provided that the particles are adsorbed on the droplets meniscus. In contrast, particles absorbed within the volume of the droplet only occasionally eject when subject to a voltage pulse. We have also performed a set of experiments measuring the critical volume and field strength E_0 at which a water droplet (no particle) becomes unstable and emits a liquid jet (Figure 29). We found a scaling law for this instability limit and have developed a theoretical model to describe it.

6.3   EFFORTS TOWARDS ENGINEERING THE PRINTHEAD

A primary engineering challenge for the DPE printer is to determine how to feed microparticles continuously to the droplet meniscus for ejection. A promising solution is to have the droplet in fluid connection with a feed channel (Figure 30). We built an experiment module to test the concept using our automated experiment apparatus. We have observed individual particles ejecting from a particle laden liquid meniscus as well as continuous particle replenishment by the channel (Figure 31).
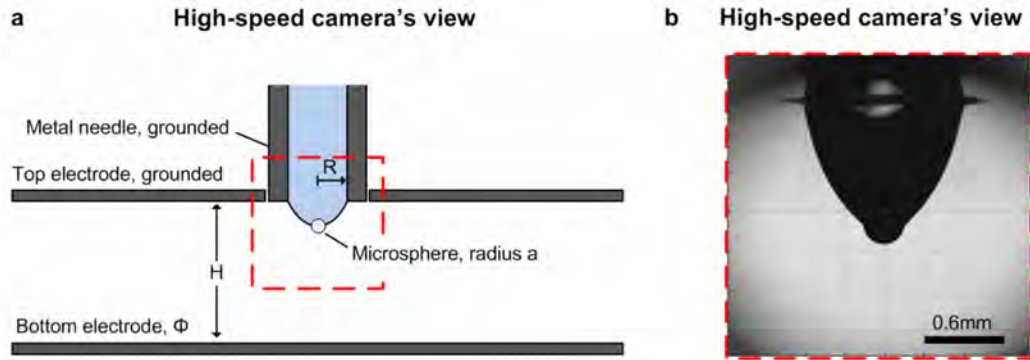
Figure 25. (a) Schematic of the experiment setup; (b) view through the high speed camera.
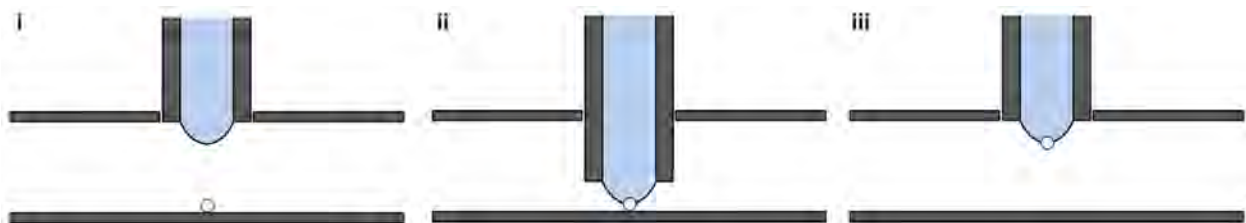
Figure 26. The procedure to prepare an experiment with a particle on the surface of the droplet comprises the following steps: (i) aligning a microparticle directly underneath the needle and droplet; (ii) lowering the needle using a vertical micrometer stage until the particle contacted the apex of the droplet; (iii) raising the needle until it is again was flush with the top electrode surface.
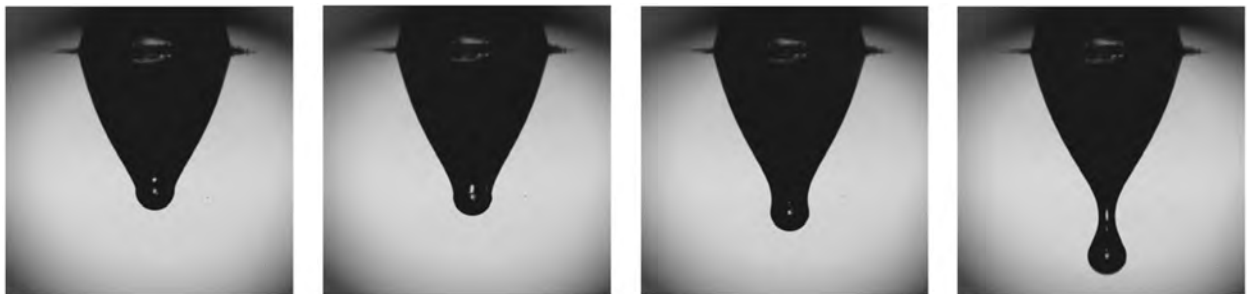
Figure 27. Frame sequence showing ejection of a single $300\,\mu m$ diameter glass particle due to an applied voltage pulse (0.55 msec between frames).
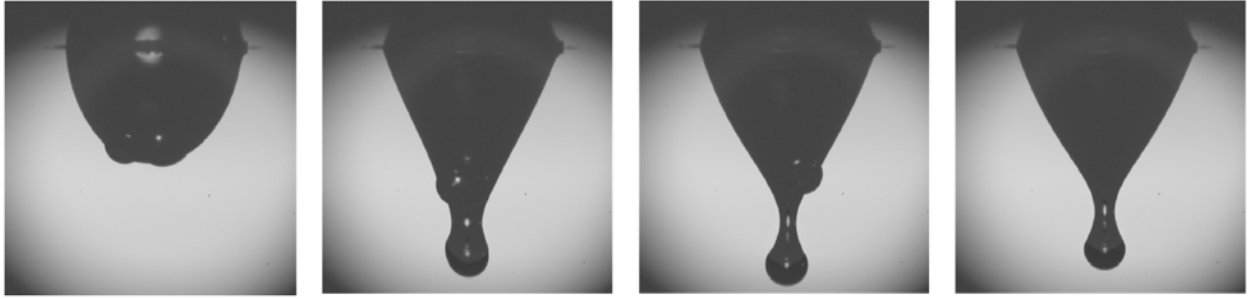
Figure 28. Frame sequence showing three $300\,\mu m$ diameter glass particles ejecting individually from a meniscus with a constant applied voltage ($200\,ms$ between frames).
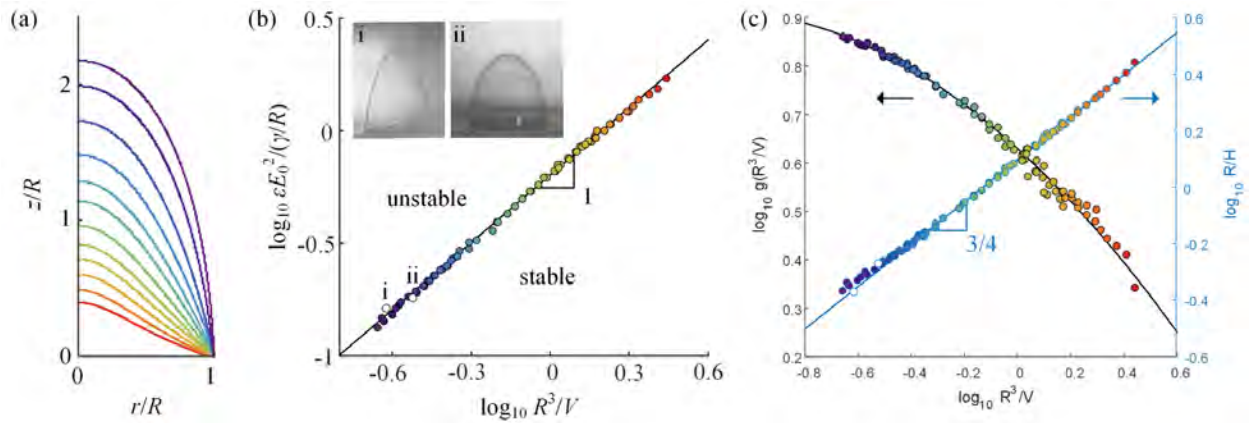
Figure 29. Experiment results for critically stable droplets before becoming unstable; colors correspond to the value $\log_{10} R^3/V$. (a) The family of critically stable droplet shapes. (b) Dimensionless plot. Black line is $R^3/V = \pi \epsilon E_0^2 R/2\gamma$. The inset pictures are the neutrally stable shapes of soap bubbles on a metal plate exposed to a uniform external field; (i) Wilson & Taylor 1925, (ii) Basaran 1990. (c) (left) $g\left(R^3/V\right)$ is the concentration of the electric field around the droplet. (right) The relationship between dimensionless parameters R^3/V and R/H, which each define the droplet shape; the blue line is $R/H = 4/3 \left(R^3/V\right)^{3/4}$.
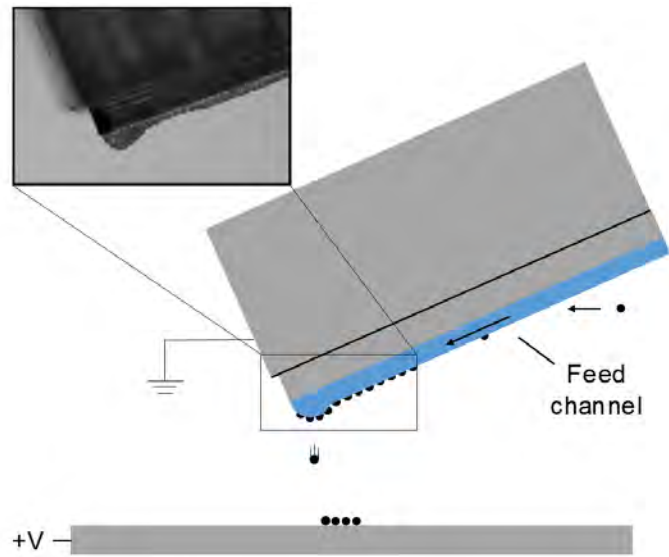
Figure 30. Channel feed schematic.
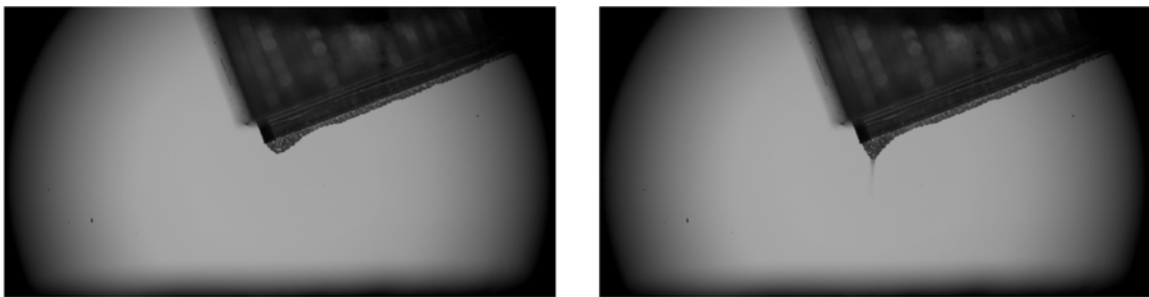
Figure 31. Ejection of an individual microparticle from particle-laden meniscus.

This page intentionally left blank.

7. CONCLUSION

During FY 2017, remarkable progress was made toward the goal of 3D printing metallic structures with high resolution positioning of both geometry and material composition. A selective laser melting machine with open architecture and basic functionality was completed and shown to be capable of fusing single layers of metal powder. The ability to form a dense, uniform powder bed with fine particles was identified as a key technology gap, and research began toward determining the particle characteristics and recoating methods that optimize powder bed properties. Mathematical models of the laser heating process were constructed in order to predict process parameters and to relate observed solidification microstructures to process parameters and thermal history. At MIT, a method was invented to eject single microparticles from fluid suspension in response to an applied voltage pulse, and the engineering began of a printhead that can deposit single microparticles with micron-level precision and high rate. The integration of all these efforts has the potential to provide unprecedented capability to 3D print metallic structures with small feature size and site-specific control of material properties, enhancing both structural response and functional capability.

Despite the successes of FY 2017, we did not propose continuation of this project in FY 2018. Started by a former Staff member, this project requires the solution of many basic research problems in several different areas, including: (1) granular flow and packing of fine particles; (2) laser processing of powder beds composed of fine particles and multiple materials; (3) reaction kinetics, wetting, and solidification of high temperature, multiphase melts; (4) electrohydrodynamic printing of single particles and its compatibility and integration with powder bed fusion. The solution of all these problems would involve substantially more time and resources than are available for NEMs Line projects. The completion of the micro-SLM alone would likely consume the majority of FY 2018. However, the micro-SLM is functional now at a basic level and could be used for the sintering or melting of single layer samples. For example, there is currently interest at the Laboratory in using laser sintering to increase the electrical conductivity of polymers loaded with high volume fractions of silver nanoparticles (for 3D printing of RF devices). Designed to be modular and flexible, the micro-SLM could also be modified or extended for many other applications.

Rather than continuing work on the micro-SLM, we recommended that the Laboratory purchase an open access, research scale SLM system. Such a system has recently been developed and brought to the market by Aconity3D, a German company with strong ties to the Fraunhofer Institute for Laser Technology, which has researched SLM since the 1990s. The Aconity3D system was recommended to us by scientists at Lawrence Livermore, who also began building a custom SLM machine before deciding that the purchase of an open access commercial system aligned more closely with their research goals. About midyear, we therefore applied FY 2017 funds toward the purchase of a Aconity3D system. This system possesses many valuable features that would have been expensive and time consuming to add to the micro-SLM, including a 400 W laser, variable beam spot size, a heated build plate, and the capability to monitor melt pool temperature. Once the system is installed, fusion of samples and material characterization can begin immediately.

Finally, we recommended that research on structural materials at the Laboratory focus on the invention of metal matrix composites (MMCs) for SLM, starting from feedstock powder that is compatible with commercial SLM systems. MMCs are the material system with the greatest potential to meet the Laboratory's pressing need for structural materials with properties superior to those of ordinary engineering alloys. In particular, many sensor and communication systems include sizable components that demand complex geometry, high stiffness, high thermal stability, and low mass. Use of MMCs in these applications would dramatically improve structural performance, but fabrication with MMCs by existing methods is slow, difficult, and limited to simple geometries. Processing MMCs with 3D printing would be ideal, but research on this topic has just begun, and not a single MMC is commercially available for 3D printing. As such, invention of MMCs for selective laser melting would enable this class of material to be used for the first time in parts requiring short production cycles and complex, optimized geometries. In this research effort, the spot size of the laser beam and the properties of the metal powder (namely particle size) should be comparable to those used in commercial SLM systems so that the materials and processing methods developed can be transferred directly to systems at the Laboratory and throughout the defense community.

A MEASURED PERFORMANCE OF PULSED LASER

TABLE A.1

Performance of Pulsed Laser as Measured by Manufacturer (Bright Solutions): Laser Power, Pulse Duration, and Pulse to Pulse Energy (E) Instability at Full Power

Pulse frequency (kHz)	Pulse duration (ps)	Power (W)	E instability (s/E_{mean})
40	480	2.1	0.050
50	506	2.25	
60	535	2.28	0.046
70	560	2.25	
80	590	2.18	0.046
100	705	1.84	0.060
150	1100	1.42	
200	1250	0.84	

This page intentionally left blank.

REFERENCES

[1] Childs T. H. C., Hauser C., Badrossamay M., 2005, "Selective laser sintering (melting) of stainless and tool steel powders: experiments and modelling," Proc. Inst. Mech. Eng. B 219 (4), 339–357.

[2] Dowden J. M., 2001, "The mathematics of thermal modeling," CRC Press, Boca Raton, FL, U. S. A.

[3] Fischer J., Kniepkamp M., Abele E., 2014, "Micro laser melting: Analyses of current potentials and restrictions for the additive manufacturing of micro structures," Proceedings of the 25th Annual International Solid Freeform Fabrication Symposium, Austin, TX, U. S. A.

[4] Matthews M. J., Guss G., Khairallah S. A., Rubenchik A. M., Depond P. J., King W. E., 2016, "Denudation of metal powder layers in laser powder bed fusion processes," Acta Mater. 114, 33–42.

[5] Rubenchik A., Wu S., Mitchell S., Golosker I., LeBlanc M., Peterson N., 2015, "Direct measurements of temperature-dependent laser aborptivity of metal powders," App. Optics 54 (24), 7230–7233.

[6] Rykalin N., Uglov A., Zuev I., Kokora A., 1995, "Laser and electron-beam treatment of metals," in: Rykalin W. (ed), Laser drilling, Chapter 9. Mir, Moscow, Russia.

[7] Shercliff H. R. and Ashby M. F., 1991, "The prediction of case depth in laser transformation hardening," Metall. Trans. A 22A, 2459-2466.

[8] Steen W. M. and Mazumder, J., 2000, "Laser material processing 4th ed.," Springer-Verlag, London, U. K.

[9] Sun S., Brandt M., Easton M., 2017, "Powder bed fusion processes: An overview," in: Brandt M. (ed), Laser Additive Manufacturing, Chapter 2. Elsevier, Duxford, U. K.

[10] Wohlers T., Campbell I., Diegel O., Kowen J., Caffrey T., "Wohlers Report 2017: 3D Printing and Additive Manufacturing State of the Industry: Annual Worldwide Progress Report," Wohlers Associates Inc., Fort Collins, CO, U. S. A.

[11] Yadroitsev I., Gusarov A., Yadroitsava I., Smurov I., 2010, "Single track formation in selective laser melting of metal powders," J. Mat. Proc. Tech. 210, 1624–1631.

[12] Yeung H., Neira J., Lane B., Fox J., Lopez F., 2016, "Laser path planning and power control strategies for powder bed fusion systems," Proceedings of the 27th Annual International Solid Freeform Fabrication Symposium, Austin, TX, U. S. A.